

Structural Insights into Ni-Stabilized Fe-Rich High-Voltage Spinel: $\text{LiNi}_x\text{Fe}_{0.5-x}\text{Mn}_{1.5}\text{O}_4$

Anna Windmüller,* Tingting Yang, Kristian Schaps, Anna Domgans, Frederik Zantis, Baolin Wu, Leyela Hassen Adem, Bikila Nagasa Olana, Chih-Long Tsai, Shicheng Yu, Luc Raijmakers, Hans Kungl, Hermann Tempel, Rafal E. Dunin-Borkowski, Shawn D. Lin, Mirijam Zobel, Bing Joe Hwang, and Rüdiger-A. Eichel

Fe-rich high-voltage spinels are attractive positive electrode materials for next-generation Li-ion batteries that offer high resource efficiency and high operating voltages. However, Fe-rich high-voltage spinels do not provide stable cycling performance, especially when compared to the Ni- and Co-rich members of the high-voltage spinel family. To understand the failure mechanism of Fe-rich high-voltage spinels, the impact of Ni stabilization on the solid solutions $\text{LiNi}_x\text{Fe}_{0.5-x}\text{Mn}_{1.5}\text{O}_4$ ($x = 0, 0.1, 0.2, 0.3, 0.4$, and 0.5) is followed. Electrochemical analysis shows that stable cycling performance can be achieved at relatively low Ni substitution ($x = 0.2$). Rietveld and pair distribution function analysis show remarkable similarity in average and local structural features, supported by 4D scanning transmission electron microscopy. The cycling mechanism of $\text{LiFe}_{0.5}\text{Mn}_{1.5}\text{O}_4$ and Ni-stabilized $\text{LiNi}_{0.2}\text{Fe}_{0.3}\text{Mn}_{1.5}\text{O}_4$ is further compared via in situ powder X-ray diffraction and in situ diffuse reflectance infrared Fourier transform spectroscopy. It is found that the presence of Ni in the electrodes leads to favorable electrolyte–electrode interactions that suppress oxidative reactions and the formation of large concentration polarizations, which is the predominant failure mechanism of $\text{LiFe}_{0.5}\text{Mn}_{1.5}\text{O}_4$.


1. Introduction

Rechargeable batteries are considered one of the key technologies to drive the global energy transition, with Li-ion batteries being the dominant technology for the last 25 years. However, in the future, next-generation and post-Li-ion technologies will be required to meet the growing and very specific needs of different sectors and applications.^[1] At the same time, the recent economic crisis and geopolitical considerations have raised concerns about resource availability and created a new awareness of local resource efficiency and strategic resource management.^[2] Spinel active materials as positive electrodes have long been discussed as favorites for the next generation of high energy density Li-ion batteries due to their fast charging capabilities and high operating voltage.^[3–5] While the well-known high-voltage $\text{LiNi}_{0.5}\text{Mn}_{1.5}\text{O}_4$ spinel, operating at 4.7 V versus

A. Windmüller, K. Schaps, A. Domgans, F. Zantis, B. Wu, C.-L. Tsai, S. Yu, L. Raijmakers, H. Kungl, H. Tempel, R.-A. Eichel
Institute for Energy Technologies (IET-1: Fundamental Electrochemistry)
Forschungszentrum Jülich
D-52425 Jülich, Germany
E-mail: a.windmueller@fz-juelich.de

T. Yang, R. E. Dunin-Borkowski
Ernst Ruska-Centre for Microscopy and Spectroscopy with Electrons (ER-C-1)
Forschungszentrum Jülich
52425 Jülich, Germany

A. Domgans, F. Zantis, B. Wu, R.-A. Eichel
Institute of Physical Chemistry
RWTH Aachen University
D-52074 Aachen, Germany

 The ORCID identification number(s) for the author(s) of this article can be found under <https://doi.org/10.1002/ssstr.202400691>.

© 2025 The Author(s). Small Structures published by Wiley-VCH GmbH. This is an open access article under the terms of the Creative Commons Attribution License, which permits use, distribution and reproduction in any medium, provided the original work is properly cited.

DOI: 10.1002/ssstr.202400691

L. H. Adem, B. N. Olana, S. D. Lin
Department of Chemical Engineering
National Taiwan University of Science and Technology
Taipei 10617, Taiwan

M. Zobel
Institute of Crystallography
RWTH Aachen University
52066 Aachen, Germany

M. Zobel
Jülich Centre for Neutron Science - Neutron Analytics for Energy Research (JCNS-3)
Forschungszentrum Jülich GmbH
Wilhelm-Johnen-Straße, 52428 Jülich, Germany

B. J. Hwang
Department of Chemical Engineering
Nano-electrochemistry Laboratory
National Taiwan University of Science and Technology
Taipei City 106, Taiwan

B. J. Hwang
Sustainable Electrochemical Energy Development Center
National Taiwan University of Science and Technology
Taipei City 106, Taiwan

Li/Li^+ , is still under intense investigation for commercialization,^[6–8] research has also long considered spinel materials that offer even higher voltages, such as Li–Co–Mn and Li–Fe–Mn spinels that operate above 5 V versus Li/Li^+ .^[4] Considering the elemental abundance and availability, especially the Fe-containing member $\text{LiFe}_{0.5}\text{Mn}_{1.5}\text{O}_4$ is an attractive alternative.^[9]

High-voltage Li–TM–Mn spinels (transition metal: $\text{TM} = \text{Co}, \text{Cr}, \text{Fe}, \text{Ni}$) are derived from Li–Mn spinels (LiMn_2O_4) by partial substitution of Mn by other TM . The obtained spinels crystallize in the $Fd\text{-}3m$ space group with a cubic close-packed oxygen sublattice.^[3,4] Following the structure type of the normal spinel, the tetrahedral and octahedral vacancies in the oxygen lattice are occupied by Li -ions and the transition metal ions, respectively. 1/2 of the tetrahedral sites are occupied by Li -ions at the $8a$ Wyckoff position and 1/2 of the octahedral sites are occupied by transition metal (TM) ions at the $16d$ Wyckoff position.^[10] Li -ion diffusion pathways in normal spinel are along the $\text{Li-}8a$ and vacant $16c$ sites.^[11] However, inverse spinels can also be formed in Li-TM compounds, where the $8a$ tetrahedral site is occupied by TM ions and the $16d$ octahedral site is occupied by up to 50% Li -ions. The degree of inversion depends on the crystal field stabilization energies for the tetrahedral and octahedral coordination of the TM -ions.^[10] Occupation of the $\text{Li-}8a$ site with TM ions directly influences the Li -ion mobility, because the $8a\text{-}16c\text{-}8a$ diffusion pathways are partially blocked^[12] but can also help to stabilize the spinel lattice during deep Li extraction.^[9,13]

Substitution of Fe^{3+} for Mn^{3+} results in the high-voltage spinel member $\text{LiFe}_{0.5}\text{Mn}_{1.5}\text{O}_4$, with $\text{Fe}^{4+/3+}$ enabling voltages around 5 V versus Li/Li^+ .^[14,15] Thus, in the $\text{LiFe}_x\text{Mn}_{2-x}\text{O}_4$ series, the high-voltage capacity due to the $\text{Fe}^{4+/3+}$ redox couple increases continuously with x . However, it has been found that the solubility limit of Fe in $\text{LiFe}_x\text{Mn}_{2-x}\text{O}_4$ is about $x = 0.4$, and the spinel starts to invert (Fe occupies the Li -site) already at $x = 0.5$,^[12,16] which leads to a continuous decrease of specific capacity and Li -ion conductivity over the series until its complete breakdown for $x = 1$.^[12] Thus, $\text{LiFe}_{0.5}\text{Mn}_{1.5}\text{O}_4$ was found to provide the highest possible capacity at 5 V versus Li/Li^+ , that is, about half of the theoretical specific capacity is gained in the 4 V region due to the $\text{Mn}^{4+/3+}$ reaction and the other half is gained in the 5 V region due to the $\text{Fe}^{4+/3+}$ reaction. Furthermore, it has been found that $\text{LiFe}_{0.5}\text{Mn}_{1.5}\text{O}_4$ suffers from severe degradation of its high-voltage capacity, when cycled to 5.2 V versus Li/Li^+ leading to the inactivity of the Fe redox only after 10–20 cycles, which hinders any practical application.^[16]

It is controversially discussed in the literature, whether the fast fading of the high-voltage capacity of $\text{LiFe}_{0.5}\text{Mn}_{1.5}\text{O}_4$ is caused by liquid electrolyte incompatibilities, structural/chemical instabilities of the spinel, or a combination of both effects.^[16–19] However, comparing the cycling performance of different high-voltage spinels, such as LiCoMnO_4 spinel,^[20,21] with the $\text{LiFe}_{0.5}\text{Mn}_{1.5}\text{O}_4$ cycling performances, raises doubts that only liquid electrolyte/electrode incompatibilities cause the fast capacity degradation of $\text{LiFe}_{0.5}\text{Mn}_{1.5}\text{O}_4$ positive electrodes. Note that F-doped LiCoMnO_4 spinels show 20% degradation after 50 cycles, while $\text{LiFe}_{0.5}\text{Mn}_{1.5}\text{O}_4$ shows 50% degradation over 50 cycles, when cycled in a similar voltage range at a $\text{C}/5$ rate. Albeit LiCoMnO_4 offers more than 80% of its capacity above 4.7 V

versus Li/Li^+ , which is beyond the stability limit of the carbonate-based liquid electrolytes.

A few studies provide evidence that Fe -containing Li–Mn spinels can achieve considerable cycling performance in the presence of other TMs . Only recently Murdock et al. highlighted the cycling stability of Li -site-deficient substituted $\text{LiFe}_x\text{Ni}_{0.5-x}\text{Mn}_{1.5}\text{O}_4$ ($x < 0.15$) spinels.^[22] Callegari et al. used Ti^{4+} doping to stabilize the spinel lattice during cycling by suppressing the Jahn–Teller effect caused by the Mn^{3+} ion and allowing an extended voltage range for deep discharge.^[23] Interestingly, Fe^{3+} substitution for Mn in LiMn_2O_4 is a well-known strategy to suppress the Jahn–Teller effect when using the $\text{Mn}^{4+/3+}$ capacity, without exploiting the $\text{Fe}^{4+/3+}$ capacity.^[24] On the other hand, moderately Fe -substituted $\text{LiNi}_{0.5}\text{Mn}_{1.5}\text{O}_4$ was shown to express enhanced electrochemical cycling and C-rate performance compared to $\text{LiNi}_{0.5}\text{MnO}_4$, due to the stabilization of the cation disordered spinel structure.^[25–28] For example, Yavuz et al. iteratively increased the Fe content in the spinel $\text{LiNi}_{0.5-x}\text{Fe}_{2x}\text{Mn}_{1.5-x}\text{O}_4$ up to ($x = 0.2$), where improved electrochemical cycle life was reported for $x = 0.1$, which was again attributed to the stabilization of the $Fd\text{-}3m$ structure via increasing the cation disorder at the $16d$ octahedral site. Yet, it has also been speculated that the low Fe^{3+} substitution leads to less electrolyte decomposition and parasitic side reactions.^[27]

While the electrochemical performance limitations of $\text{LiFe}_{0.5}\text{Mn}_{1.5}\text{O}_4$ spinel have been well reported and some doping strategies have been documented, a comprehensive insight and explanation for the severe electrochemical performance degradation observed with the $\text{LiFe}_{0.5}\text{Mn}_{1.5}\text{O}_4$ spinel is, to our knowledge, lacking. Here, we use Ni as a stabilizing substituent to systematically study the solid-solution $\text{LiNi}_x\text{Fe}_{0.5-x}\text{Mn}_{1.5}\text{O}_4$ comprehensively from an electrochemical and structural point of view. We consider average structural information as well as local structural information and the Li -concentration-dependent structural evolution to understand possible effects on the electrochemical performance. We aim to further understand the failure mechanisms of the Fe spinels and provide insights into possible advances through doping and substitution strategies.

2. Results and Discussion

2.1. Basic Material Characterization

The targeted phase is spinel in the space group $Fd\text{-}3m$ (Figure 1a) along the composition line with the end members $\text{LiNi}_{0.5}\text{Mn}_{1.5}\text{O}_4$ and $\text{LiFe}_{0.5}\text{Mn}_{1.5}\text{O}_4$ as $\text{LiNi}_x\text{Fe}_{0.5-x}\text{Mn}_{1.5}\text{O}_4$ with an x step of 0.1, yielding 6 samples (Figure 1b). The recorded powder X-ray diffraction (PXRD) patterns (Figure 1c) can be indexed to the desired cubic $Fd\text{-}3m$ spinel structure. Superlattice reflections ($P4_332$) or reflections from tetragonal distortion ($I4_1amd$) are not observed for any of the compounds. An obvious shift in peak positions toward higher angles is noted with increasing Ni , while only very small contributions of well-known secondary phases like Li_2MnO_3 and NiO can be found,^[29–32] with NiO in $\text{LiNi}_{0.5}\text{Mn}_{1.5}\text{O}_4$ being the most obvious. See Figure S1, Supporting Information, for a detailed view of the PXRD results. A quantitative approach based on Rietveld and pair distribution

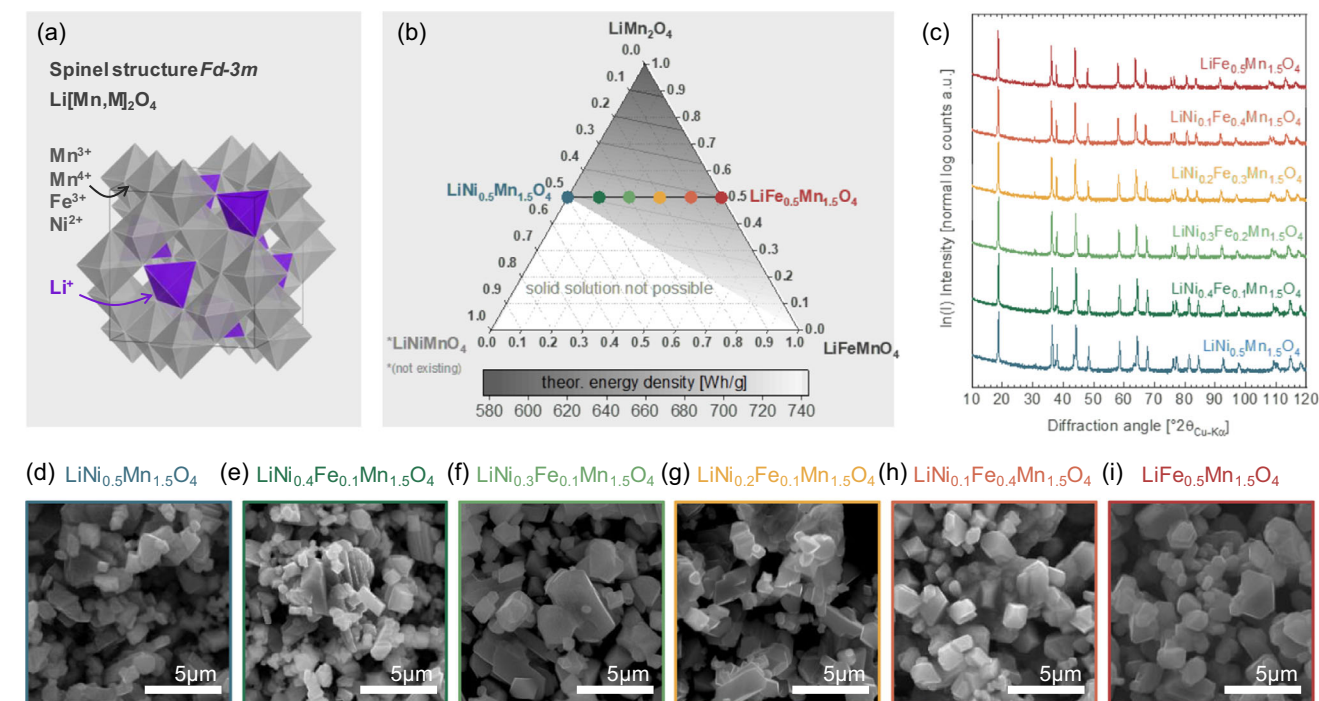


Figure 1. a) Spinel structure with Li sitting in tetrahedral $8a$ positions (in purple) and transition metals sitting in octahedral $16d$ positions. b) Targeted solid solution compounds along the tie line $\text{LiNi}_{0.5}\text{Mn}_{1.5}\text{O}_4$ – $\text{LiFe}_{0.5}\text{Mn}_{1.5}\text{O}_4$ (substitution of Fe by Ni with a step of $x = 0.1$ mol per formula unit). c) Obtained PXRD patterns of the powder samples after synthesis. d–i) SEM images of obtained powder samples after synthesis: d) $x = 0.5$; e) $x = 0.4$; f) $x = 0.3$; g) $x = 0.2$; h) $x = 0.1$; i) $x = 0$.

function analysis follows in subsequent sections. Scanning electron microscopy (SEM) analysis shows similar particle morphologies with well-crystallized facets and particle sizes around $1\ \mu\text{m}$ (Figure 1d–i). Chemical characterization, as shown in Figure 2a, indicates that the targeted cation stoichiometry was achieved for all samples (see also Table S2, Supporting Information).

From the PXRD results and the chemical analysis, it is obvious that a solid solution along the tie line $\text{LiNi}_{0.5}\text{Mn}_{1.5}\text{O}_4$ – $\text{LiFe}_{0.5}\text{Mn}_{1.5}\text{O}_4$ could be successfully achieved. It is known that the valence distribution in $\text{LiNi}_{0.5}\text{Mn}_{1.5}\text{O}_4$ is $\text{Li}^+\text{Ni}_{0.5}^{2+}\text{Mn}_{1.5}^{4+}\text{O}_4$ and in $\text{LiFe}_{0.5}\text{Mn}_{1.5}\text{O}_4$ it is $\text{Li}^+\text{Fe}_{0.5}^{3+}\text{Mn}_{0.5}^{3+}\text{Mn}^{4+}\text{O}_4$.^[16,33] This implies the substitution mechanism of 1 Ni^{2+} and 1 Mn^{4+} for 1 Fe^{3+} and 1 Mn^{3+} as $\text{Li}^+\text{Ni}_x\text{Fe}_{0.5-x}\text{Mn}_{0.5-x}^{3+}\text{Mn}_{1+x}^{4+}\text{O}_4$. Based on the proposed substitution mechanism and assuming oxygen stoichiometry, the evolution of the expected valence states along the solid solution can be anticipated, as is summarized in Figure 2b. It is important to note, how in this scenario the Mn valences change with x , to maintain the charge balance upon the substitution of Fe^{3+} for Ni^{2+} . This results in the conversion of the electrochemically inactive Mn^{4+} to an electrochemically active Mn^{3+} in the corresponding voltage range. Active Fe^{3+} and Mn^{3+} with a 1-electron redox each are replaced by active Ni^{2+} with a 2-electron redox. Accordingly, the theoretical capacities of the individual spinel compounds are expected to show almost identical values of about $145\ \text{mAh g}^{-1}$ for the extraction of 1 Li per formula unit from the tetrahedral site.

2.2. Electrochemical Analysis

Figure 2c–e shows the results of the electrochemical analysis of all the spinel electrodes. The cyclic voltammetry (CV) scan for $\text{LiFe}_{0.5}\text{Mn}_{1.5}\text{O}_4$ displays the expected activity of $\text{Mn}^{4+/3+}$ (4.0 V versus Li/Li^+) and $\text{Fe}^{4+/3+}$ (5.1 V versus Li/Li^+) redox couples with similar peak currents of $30\ \text{mA g}^{-1}$ in the oxidation reaction and $28\ \text{mA g}^{-1}$ in the reduction reaction, as expected from the cation stoichiometry and in agreement with the literature.^[16,34,35] The Ni-substituted samples show a stepwise increase in the activity of the two-electron process provided by the $\text{Ni}^{4+/3+}/^{2+}$ redox couple at 4.7 V versus Li/Li^+ ,^[36] while the redox activity of $\text{Fe}^{4+/3+}$ and $\text{Mn}^{4+/3+}$ gradually decreases (Figure 2c). This observation agrees with the calculated valence states in (Figure 2b). However, we observe that the Ni-rich endmember $\text{LiNi}_{0.5}\text{Mn}_{1.5}\text{O}_4$ displays an unexpected contribution of the $\text{Mn}^{4+/3+}$ redox couple at 4 V versus Li/Li^+ . From the stoichiometry and the expected valence states, this compound should not contain any Mn^{3+} . This contradiction can be explained by the presence of secondary phases, such as NiO , which depletes the $\text{LiNi}_{0.5}\text{Mn}_{1.5}\text{O}_4$ in Ni and changes the Ni/Mn ratio in the spinel thus allowing the presence of Mn^{3+} in an overall charge-neutral spinel compound, which is a common observation in the literature.^[22,37]

The discharge curves for the first 2 cycles at a C/5 rate for the samples $x = 0.0$ to 0.5 are displayed in Figure 2d. As expected from the similar theoretical capacities for all samples, the experimentally determined discharge capacities at a C/5 rate all fall in

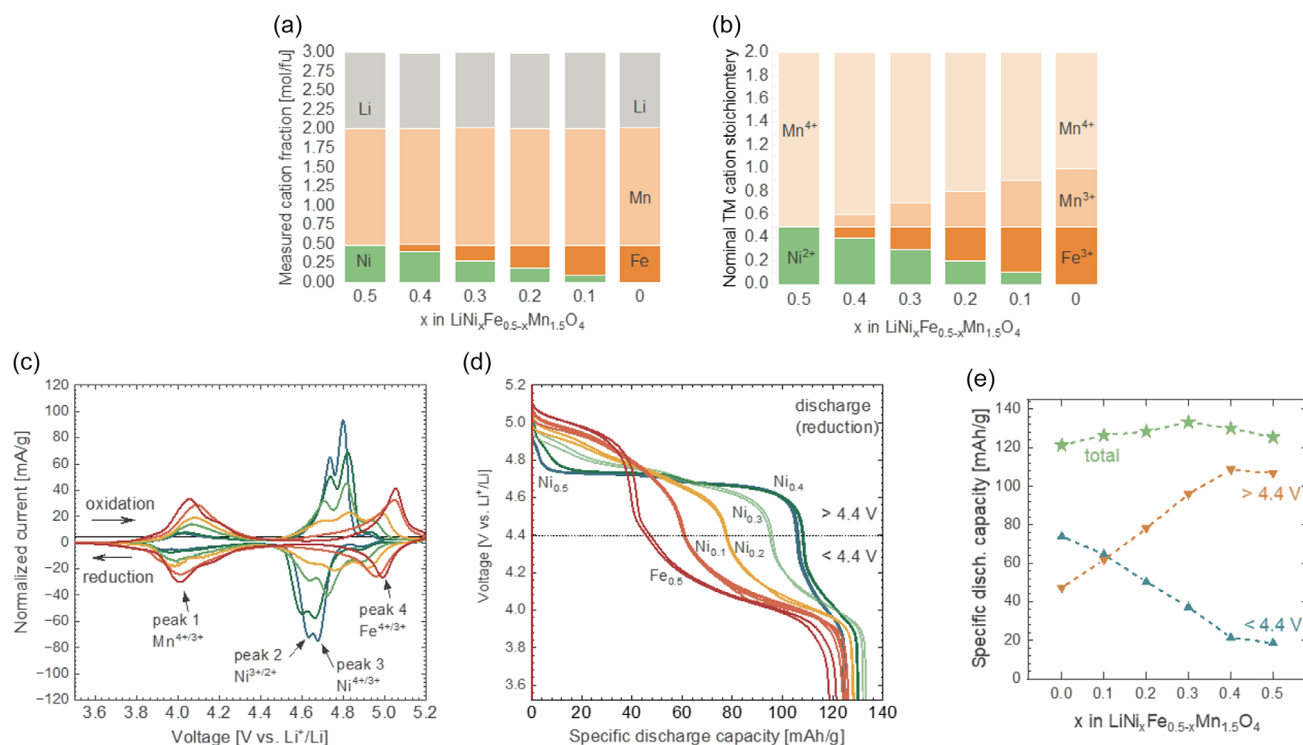


Figure 2. Chemical and initial electrochemical analysis for all samples $\text{LiNi}_x\text{Fe}_{0.5-x}\text{Mn}_{1.5}\text{O}_4$ ($x = 0, 0.1, 0.2, 0.3, 0.4$, and 0.5): a) Results from the chemical analysis of cations Li, Fe, Mn, and Ni by ICP-OES (values in Table S1, Supporting Information). b) calculated valence states based on the measured cation fractions and assuming oxygen stoichiometry. The valence states of Fe for $x = 0$ were confirmed by Mössbauer spectroscopy previously.^[16] c) CV at a scan rate of 0.02 mV s^{-1} in the voltage range $3.5\text{--}5.2 \text{ V}$ versus Li/Li^+ in the first 2 cycles. d) Discharge curves in the 1st and 2nd cycle from galvanostatic charge–discharge experiments at a C rate of C/5 in the voltage range $3.5\text{--}5.2$ versus Li/Li^+ . e) Evolution of discharge capacities above and below 4.4 V versus Li/Li^+ as a function of Ni content (x).

the range of about $120\text{--}133 \text{ mAh g}^{-1}$, which is also consistent with the initial discharge capacities reported in the literature.^[16,27,28] Similar to the CV results, a stepwise decrease of the redox activities of the $\text{Mn}^{4+/3+}$ can be observed below 4.5 V versus Li/Li^+ , while above 4.5 V versus Li/Li^+ the activities in terms of measured capacities increase stepwise with Ni^{2+} substitution in the spinel compound (Figure 2e). The CV curves show the presence of distinct peaks for $\text{Mn}^{4+/3+}$, $\text{Ni}^{2+/2+}$, and $\text{Fe}^{4+/3+}$ specifically for the Fe-rich and Ni-rich members of the series. We observed that the CV peaks broadened for $x = 0.2$ and 0.3 , and thus, we also observed a “sloppy” discharge profile with less pronounced plateaus for $x = 0.2$ and 0.3 . As can be seen from the CVs, the behavior of $\text{LiNi}_{0.5}\text{Mn}_{1.5}\text{O}_4$ deviates from the general trend. Here, no capacity is expected to be below 4.5 V versus Li/Li^+ for a nominal stoichiometric compound of $\text{LiNi}_{0.5}\text{Mn}_{1.5}\text{O}_4$. In the literature, $\text{Mn}^{4+/3+}$ capacities in $\text{LiNi}_{0.5}\text{Mn}_{1.5}\text{O}_4$ are known to be caused by oxygen vacancies, which can give rise to a substantial capacity of about $5\text{--}10 \text{ mAh g}^{-1}$ due to the $\text{Mn}^{4+/3+}$ redox.^[38,39] However, considering the larger capacity of the $\text{Mn}^{4+/3+}$ redox ($\approx 20 \text{ mAh g}^{-1}$) for $x = 0.5$ and $x = 0.4$ samples in this study, the recorded capacities below 4.5 V versus Li/Li^+ must—to a large extent—be explained by the changed Ni/Mn ratio in the presence of secondary phases, as discussed for the CV results.

Besides the changes that can be explained by the changing Ni/Fe ratios and secondary phases, we observe that the potential

window for accessing the capacities of the compounds changes with the Ni substitution level. While for $\text{LiFe}_{0.5}\text{Mn}_{1.5}\text{O}_4$ almost the full capacity from the $\text{Fe}^{4+/3+}$ high-voltage redox couple can only be exploited above 5.0 V versus Li/Li^+ , for Ni-doped counterparts the full capacities can be easily achieved below 5.0 V versus Li/Li^+ . For the compounds with $x = 0.2$ ($=0.2 \text{ Ni per FU}$), this means that the capacity of $0.3 \text{ Fe}^{4+/3+}$ per FU ($\approx 75 \text{ mAh g}^{-1}$) can be exploited at much lower potentials than for $\text{LiFe}_{0.5}\text{Mn}_{1.5}\text{O}_4$. This property may have significant implications for the cycling stability of $\text{Li}(\text{Ni,Fe,Mn})_2\text{O}_4$ spinels as a function of their cut-off voltage and Fe-content, as is already evident from reports in the literature.^[16,27,40]

Figure 3a compares the discharge capacities within the first 35 cycles of all samples in the potential window of $3.5\text{--}5.2 \text{ V}$ versus Li/Li^+ . There are significant differences in the cycling stability of the different samples. For $\text{LiFe}_{0.5}\text{Mn}_{1.5}\text{O}_4$, fast degradation upon cycling is observed, similar to literature reports.^[16] We observe that the discharge capacity of $\text{LiFe}_{0.5}\text{Mn}_{1.5}\text{O}_4$ decreases to about 50% of its initial capacity after 15 cycles, while it remains constant at 60 mAh g^{-1} after the 15th cycle and until the end of the experiment. We further observed that the cycling stability is significantly enhanced by substituting 0.1 mol Ni^{2+} per formula unit in $\text{LiNi}_x\text{Fe}_{0.5-x}\text{Mn}_{1.5}\text{O}_4$. $\text{LiNi}_{0.1}\text{Fe}_{0.4}\text{Mn}_{1.5}\text{O}_4$ still delivers 90 mAh g^{-1} after 35 electrochemical cycles, which is 70% of its discharge capacity retention. For $\text{LiNi}_{0.2}\text{Fe}_{0.3}\text{Mn}_{1.5}\text{O}_4$, the

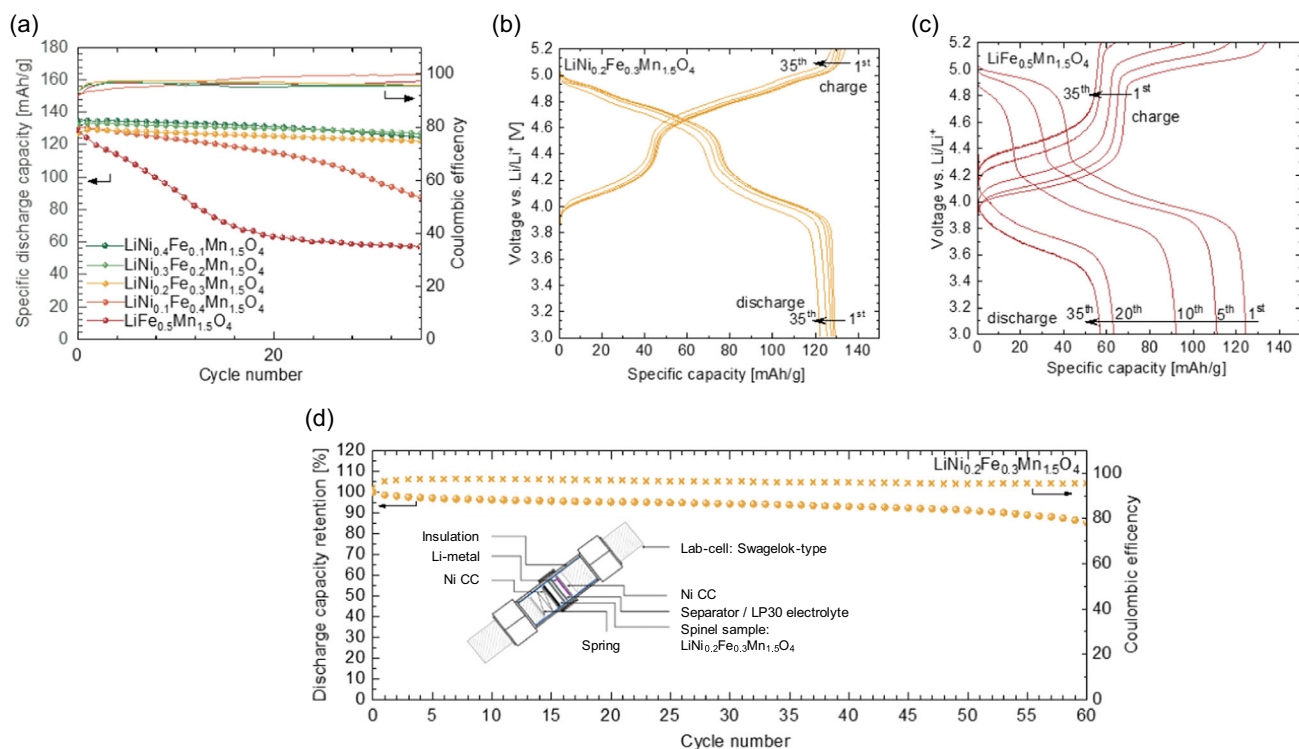


Figure 3. a) Discharge capacity (dots) and efficiency (crosses) over cycle number for galvanostatic charge–discharge at a C/5 rate over 35 cycles for $\text{LiNi}_x\text{Fe}_{0.5-x}\text{Mn}_{1.5}\text{O}_4$ ($x = 0, 0.1, 0.2, 0.3, 0.4$, and 0.5). Individual charge and discharge curves for b) $x = 0.2$ and c) $x = 0$. d) Discharge capacity and efficiency over cycle number for galvanostatic charge–discharge at a C/5 rate over 60 cycles for $x = 0.2$.

electrochemical cycling stability is dramatically improved, with a discharge capacity of 135 mAh g^{-1} recorded after 35 cycles, corresponding to 97% of the discharge capacity retention. A further improvement of the electrochemical cycle stability is negligible when the substitution is increased to 0.3 and 0.4 mol Ni^{2+} per formula unit.

Figure 3b,c compares the evolution of the charge and discharge curves for $x = 0.2$ and $x = 0$, respectively. As can be expected from the stable cycling performance, the individual charge and discharge curves for $\text{LiNi}_{0.2}\text{Fe}_{0.3}\text{Mn}_{1.5}\text{O}_4$ lay almost on top of each other. The curves at higher cycles differ from the initial curves only by a shift to lower potentials (discharge) and higher potentials (charge), indicating an overall cell polarization that builds up over the cycle numbers. The recorded cell polarization from the 1st to the 35th cycle is 0.1 V. The build-up of cell polarization over cycling is much more severe for $\text{LiFe}_{0.5}\text{Mn}_{1.5}\text{O}_4$. Here, we observe a cell polarization from the 1st to the 35th of almost 1 V. At the same time, we see that $\text{LiFe}_{0.5}\text{Mn}_{1.5}\text{O}_4$ initially has a charge capacity of about 73 mAh g^{-1} below 4.7 V versus Li/Li^+ , where 4.7 V versus Li/Li^+ marks the stability limit of the liquid electrolyte. However, it reaches another 47 mAh g^{-1} above 4.7 V versus Li/Li^+ . Obviously, this high-voltage capacity decreases rapidly with the build-up of the cell polarization. In fact, the capacity above 4.7 V versus Li/Li^+ becomes inaccessible after about 15 cycles, while we see that the Coulombic efficiency (Figure 3a) stabilizes at 99% (initially 97%).

The significant stabilization of the cycling performance for $x = 0.2$ already is unexpected especially considering the very similar capacities above 4.7 V versus Li/Li^+ , which is the upper stability limit of the liquid electrolyte (in this case conventional LP30, 1 M LiPF_6 in EC/DMC). However, the discharge capacities recorded above that limit (4.7 V versus Li/Li^+) based on the experiment in Figure 2d are 40, 48, 54, and 59 mAh g^{-1} for $x = 0, 0.1, 0.2$, and 0.3 , respectively. Thus, it is not directly plausible to explain the fast degradation of $\text{LiFe}_{0.5}\text{Mn}_{1.5}\text{O}_4$ solely by liquid electrolyte decomposition and subsequent parasitic reactions.

Stable cycling performance has previously been reported for low-level Fe-substituted $\text{LiNi}_{0.42}\text{Fe}_{0.16}\text{Mn}_{1.42}\text{O}_4$ and $\text{LiNi}_{0.34}\text{Fe}_{0.16}\text{Mn}_{1.5}\text{O}_4$ yet below 5.0 V versus Li/Li^+ ,^[26] without accessing a large part of the $\text{Fe}^{4+/3+}$ capacity. Similarly, $\text{LiNi}_{0.3}\text{Fe}_{0.4}\text{Mn}_{1.3}\text{O}_4$ was reported to have a decent cycling stability at capacity retention of 90% after 300 cycles yet again only up to a cutoff at 5.0 V versus Li/Li^+ .^[27] In our previous study, we demonstrated the effect of changing the upper cutoff voltage from 5.0 to 5.2 V versus Li/Li^+ (to access more of the $\text{Fe}^{4+/3+}$ capacity) which has a significant impact on the cycling stability even for $\text{LiFe}_{0.5}\text{Mn}_{1.5}\text{O}_4$: The capacity retention after 20 cycles changes from 92 to 50%, when changing the upper cutoff voltage from 5.0 to 5.2 V versus Li/Li^+ .^[16] In this study however, we can achieve a stabilization of cycling performance by lowering the potential for $\text{Fe}^{4+/3+}$ exploitation below 5.0 V versus Li/Li^+ . Aware of the limitations of the liquid electrolyte and without

attempting to improve cell design or liquid electrolyte formulation (a stable one up to 5.0 V versus Li/Li⁺ has yet to be found), we have cycled the LiNi_{0.2}Fe_{0.3}Mn_{1.5}O₄ for over 60 cycles with 80% capacity retention, as depicted in Figure 3d.

2.3. Rietveld and PDF Analysis

The reason for the enhanced cycling performance of LiNi_{0.2}Fe_{0.3}Mn_{1.5}O₄ compared to unsubstituted LiFe_{0.5}Mn_{1.5}O₄ is unknown till this point. We speculate that the improved cycling stability may be due to improved structural stability resulting in improved cycling mechanisms during cycling. Especially for LiNi_{0.5}Mn_{1.5}O₄, it is known that its defect structure can change the cycling mechanism from a so-called 2-phase mechanism to a solid-solution mechanism.^[33] The changed mechanism has a tremendous impact on cycling stability, with the solid solution mechanism resulting in improved cycling stability due to the suppression of structurally induced microstructural degradation due to phase transitions. This effect is closely related to the defect and crystal chemistry of the spinel phase itself. Therefore, the following advanced structural analysis was performed to understand the origin of the improved cycling stability from a structural point of view.

Figure 4 shows the results of the Rietveld analysis of the 6 spinel samples investigated, based on the diffraction patterns obtained with a hard monochromatic X-ray source (Ag-Kα₁). Figure 4a displays an example fit for LiNi_{0.1}Fe_{0.4}Mn_{1.5}O₄, and the Supporting Information (Figure S2) provides the visualization of the fits of the other 5 samples. In the Rietveld refinement, spinel with the general composition Li^{8a}(Fe,Ni,Mn)₂^{16d}O₄ in the space group *Fd-3m* with a lattice parameter of 8.250 Å was used as a starting model. It is known that the tetrahedral (8a) site can

be occupied by Li-ions or Fe-ions and the octahedral (16d) site can be occupied by TM-ions or Li-ions (Figure 4b). As the partial occupation of Fe³⁺ at 8a sites in LiFe_{0.5}Mn_{1.5}O₄ was previously identified by Mößbauer spectroscopy,^[16] we considered Fe occupancy also at 8a sites (constraining the occupancy to Fe + Li = 1). Li occupancy on 16d sites was included first, by constraining the occupancy to TM + Li = 1. However, the Li occupancy at 16d was later neglected in the model, because it never refined away from 0. As such, spinel inversion (occupancy of Fe at 8a), lattice parameters, and $x = y = z$ atomic fractions of O were the main structural parameters that were refined. With the given model the fits converged well, yielding weighted pattern residuals (R_{wp}) below 5% and goodness of fit values (χ^2) below 4.6 (exact values as a reference in Figure S2, Supporting Information, all refined parameters are in Table S2, Supporting Information).

The evolution of the lattice parameters as a function of x (Ni in LiNi_{*x*}Fe_{0.5-*x*}Mn_{1.5}O₄) shows a decreasing trend. The decrease is consistent with the proposed substitution mechanism of 1 Ni²⁺ and 1 Mn⁴⁺ for 1 Fe³⁺ and 1 Mn³⁺. Here, Mn⁴⁺ (0.53 Å for VI-coordinated, high-spin) is rather small compared to that of Fe³⁺ (0.645 Å for VI-coordinated, high-spin) and Mn³⁺ (0.645 Å for VI-coordinated, high-spin) as well as that of Ni²⁺ (0.69 Å for VI-coordinated, high-spin). Thus, the changing cation ratios at the octahedral site with x in LiNi_{*x*}Fe_{0.5-*x*}Mn_{0.5-*x*}³⁺Mn_{1+*x*}O₄ decrease the volume of the octahedral coordination polyhedral and thus the overall volume of the unit cell. The trend is not strictly linear, for high x (high Ni content) the decrease in lattice parameters becomes less obvious, and almost identical lattice parameters are achieved for LiNi_{0.4}Fe_{0.1}Mn_{1.5}O₄ and LiNi_{0.5}Mn_{1.5}O₄. The deviation from the linear trend correlates with the appearance of larger amounts of the NiO secondary phase (quantifies to 1.5 wt% for LiNi_{0.4}Fe_{0.1}Mn_{1.5}O₄ and 4.0 wt%

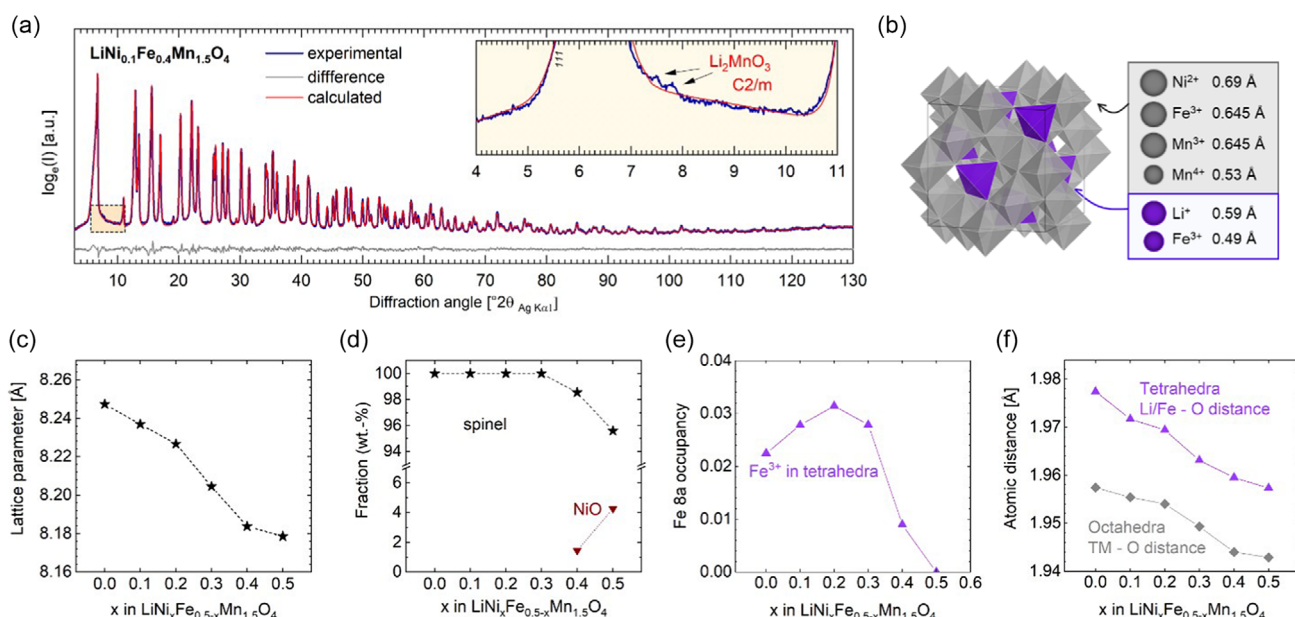


Figure 4. Results from Rietveld analysis based on Ag Kα₁ PXRD data for LiNi_{*x*}Fe_{0.5-*x*}Mn_{1.5}O₄ ($x = 0, 0.1, 0.2, 0.3, 0.4$, and 0.5): a) Example fit for $x = 0.1$, the inset shows identified impurity reflections. b) Spinel structure and indication of specific ionic radii for tetrahedral and octahedral coordination. c–f) Refined parameters as a function of x : c) lattice parameters; d) secondary phase wt% fractions; e) Fe occupancy at 8a; and f) calculated bond distances from refined lattice parameters and fractional coordinate of the 32e site (see Table S2, Supporting Information for parameter values).

for $\text{LiNi}_{0.5}\text{Mn}_{1.5}\text{O}_4$, Figure 4c,d). Although Li_2MnO_3 may be present in the sample (see inset in Figure 4a), it was not possible to adequately fit Li_2MnO_3 within the fit. This is primarily due to the very low intensity and limited number of independent Li_2MnO_3 reflections. Li_2MnO_3 is structurally similar to spinel, and the majority of its primary Bragg peaks overlap those of spinel. We will discuss the presence of Li_2MnO_3 further in the following pair distribution function analysis.

In the literature, rocksalt-type NiO phases and monoclinic Li_2MnO_3 secondary phases are well known to coexist with $\text{Li}(\text{Ni,Mn})_2\text{O}_4$ spinels.^[29,31] However, especially for the popular $\text{LiNi}_{0.5}\text{Mn}_{1.5}\text{O}_4$ member, sophisticated synthesis routes exist that yield higher purity spinel samples.^[41] These synthesis routes differ from the one chosen here in terms of temperature, atmosphere, or even wet chemical versus solid-state approaches. The synthesis route in this study was optimized to achieve an optimized phase purity for the Fe-rich $\text{LiFe}_{0.5}\text{Mn}_{1.5}\text{O}_4$ member. To avoid microstructural changes (due to different temperature treatments or synthesis routes) that would impact the electrochemical performance,^[28] the same synthesis protocol was applied to all members of the series. Hence, our chosen synthesis approach via solid-state reaction at 800 °C produces highly phase pure Fe-rich Li–Fe–Mn–O spinels but has drawbacks in terms of phase purity for the Ni-rich members.

Figure 4e shows the results of the refined Fe occupancy at site 8a, which is an indicator of spinel inversion. As can be seen, the spinel inversion peaks at $x = 0.2$ ($\text{LiNi}_{0.2}\text{Fe}_{0.3}\text{Mn}_{1.5}\text{O}_4$), with 3%

Fe occupancy at the 8a site. Fe^{3+} (as previously identified at $8a^{[16]}$) has an ionic radius of 0.49 Å (for IV HS) and is significantly smaller than Li^+ (0.59 Å for IV). Thus, it also changes the volume of the tetrahedral coordination polyhedral and thus impacts the overall unit cell dimensions. The trend of the bond lengths in the tetrahedral and octahedral coordination polyhedra is shown in Figure 4f, which demonstrates that the impact of Mn^{4+} within the octahedra determines the overall dimensions of both polyhedra.

Comparison of the average structural properties, especially for the apparent phase pure $\text{LiFe}_{0.5}\text{Mn}_{1.5}\text{O}_4$, $\text{LiNi}_{0.1}\text{Fe}_{0.4}\text{Mn}_{1.5}\text{O}_4$, $\text{LiNi}_{0.2}\text{Fe}_{0.3}\text{Mn}_{1.5}\text{O}_4$, and $\text{LiNi}_{0.3}\text{Fe}_{0.2}\text{Mn}_{1.5}\text{O}_4$, does not provide a readily available explanation for the very different electrochemical performances. Structural properties that typically enhance electrochemical performance, such as wider lattice dimensions and reduced spinel inversion, which facilitate Li-ion diffusion from 8a to vacant 16c to 8a sites,^[12,42] even show reverse trends to the observed trends in electrochemical performance. On the other hand, it is known that defect structural properties, such as cation order at octahedral sites and anionic defects, have a strong influence on the electrochemical properties.^[43,44]

Rietveld analysis provides a very good overview of the average structural properties of spinel samples. However, it lacks information about the spinel defect structure, which is an important factor in evaluating the electrochemical performance of the material. Thus, the PDF was calculated from the obtained hard X-ray scattering data,^[45] for each sample to investigate the local structure. Figure 5 gives an overview of the results

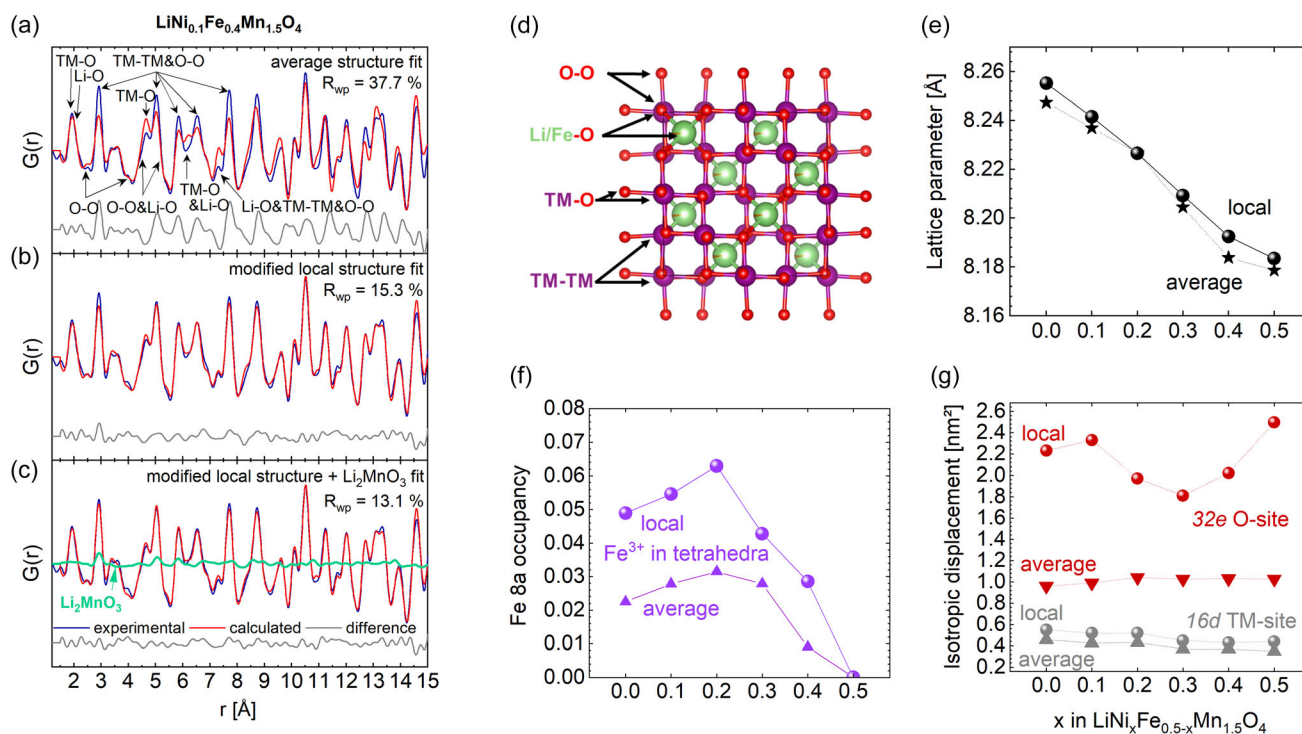


Figure 5. Results from PDF analysis based on Ag $K\alpha_1$ PXRD data for $\text{LiNi}_x\text{Fe}_{0.5-x}\text{Mn}_{1.5}\text{O}_4$ ($x = 0, 0.1, 0.2, 0.3, 0.4$, and 0.5): a–c) Example fits for $x = 0.1$ for 3 different fitting models: a) average structure only, b) average structure + B_{iso} + Fe occupancies at 8a, and c) full model including Li_2MnO_3 fractions under spherical damping (finite crystalline domain size). d) visualization of atomic pairs in the average spinel structure for Rietveld refined $\text{LiNi}_{0.1}\text{Fe}_{0.4}\text{Mn}_{1.5}\text{O}_4$. e–g) Refined parameters from the full model in (c) as a function of x in comparison to the average structure parameters from Rietveld: e) lattice parameters, f) Fe occupancy at 8a; and g) isotropic displacement parameters.

of the PDF analysis. Figure 5a–c displays an example fit for $\text{LiNi}_{0.1}\text{Fe}_{0.4}\text{Mn}_{1.5}\text{O}_4$ with three different fitting models. The Supporting Information (Figure S3–S6) provides visualization of the fits of all samples for the same models. Figure 5d shows the average spinel structure as obtained from Rietveld analysis with the nearest neighbor pairs indicated.

The first model (Figure 5a) takes the determined average structure from the Rietveld analysis as a model and allows only the refinement of the correlated motion term δ_2 of the nearest neighbors atoms (as described by Jeong et al.^[46]), the lattice parameter, and the PDF scale factor (model PDF to experimental PDF). As is apparent, the fit is not optimal and important features in the PDF, such as the TM–TM and O–O distances, are poorly described. The second model (Figure 5b) allows for the refinement of the thermal/statistical displacement for TM and O at $8a$, $16e$, and $32e$ respectively. It also allows the refinement of the Fe occupancy at the $8a$ site. As can be seen and additionally evidenced by the reduction of the goodness-of-fit parameter R_{wp} from 37.7 to 15.3%, a significant improvement of the fitting quality is achieved, not only for the example in Figure 5b for $x = 0.1$, but also for the other samples (Figure S4, Supporting Information). The third model (Figure 5c) considers the possible contribution of the well-known Li_2MnO_3 secondary phase. Its presence is already indicated in the Bragg data (Figure 5a, inset), but it could not be successfully included in a quantitative phase analysis based on the Bragg data. Figure 5c shows that its contribution to the PDF can very well describe the missing TM–TM and O–O correlations at 2.9 and 5.0 Å in the PDF data for $\text{LiNi}_{0.1}\text{Fe}_{0.4}\text{Mn}_{1.5}\text{O}_4$. Similarly, the PDF fit of the other samples (Figure S5 and S6, Supporting Information) improves after the Li_2MnO_3 contributions are introduced and the fit in general improves with final R_{wp} values below 13.0% (list of refined parameters from the third model for all samples in Table S3, Supporting Information).

Figure 5e–g gives an overview of the refined local structural parameters in the third model compared to the determined average structural parameters. While the refined lattice parameters are similar for the average and the local structure (Figure 5e), the other parameters (spinel inversion and isotropic displacement) show significant discrepancies. The spinel inversion (or Fe occupancy at $8a$) is more than doubled at the local scale (Figure 5f)—probably indicating Fe clustering at the local scale. Interestingly, the isotropic displacement parameters for O at the $32e$ site also show much higher values at the local scale (PDF fit from 1.5 to 15 Å) (Figure 5g). It can be interpreted as statistical displacement rather than thermal displacement. This phenomenon can be attributed to the bond length variations and local coordination distortions introduced into the spinel lattice by the various transition metals occupying the $16d$ site, such as Ni^{2+} , Fe^{3+} , Mn^{3+} , and Mn^{4+} . It suggests distortions in the oxygen anionic lattice induced by these differently sized cations.^[47] While the position of the cations appears to remain largely unchanged on both the local and average scales, their sizes and different electronic configurations are most obviously compensated for by the displacement of the oxygen from its ideal/average position.

At the same time, Li_2MnO_3 is detected for all samples at the local scale (Figure 5g). The best description is achieved with Li_2MnO_3 nanoscale phases with a domain size of about

1–4 nm. The finite size of this phase was modeled by spherical damping.^[48] The damping term was determined from an initial fit to 30 Å and fixed in subsequent refinements, which run only to 15 Å. The damping term was kept fixed until all other parameters converged. It was not released until the final iteration. The presence of Li_2MnO_3 again suggests oxygen depletion/deficiency of the main spinel phase. Li–Mn spinels release oxygen from the crystal lattice depending on the temperature and atmospheric conditions.^[49] Due to the synthesis at 800 °C in the air in this study, the formation of oxygen deficiencies and subsequent Li_2MnO_3 formation is highly plausible. It agrees with previous observations, where oxygen defects of about 2–3% were observed, with coexisting Li_2MnO_3 .^[21,50] Furthermore, it has been shown that Li_2MnO_3 exists as nanoscale segregations in the Li–Mn system.^[51] However, it is present in very small amounts and is therefore difficult to detect from its Bragg peaks, which are relatively broad due to the nanoscale nature of the phase. This is consistent with the results of our PXRD analysis, where we identified only very low intensity and broad reflections of Li_2MnO_3 .

To prove the existence of nanoscale Li_2MnO_3 being present in the samples, the atomic high angle annular dark field scanning transmission electron microscopy (HAADF-STEM) and 4D scanning transmission electron microscopy (4D-STEM) techniques were performed to characterize the structure of the $\text{LiNi}_{0.2}\text{Fe}_{0.3}\text{Mn}_{1.5}\text{O}_4$ sample (Figure 6a), in which almost no Li_2MnO_3 secondary phase reflection could be detected (Figure S1, Supporting Information). To further analyze the $\text{LiNi}_{0.2}\text{Fe}_{0.3}\text{Mn}_{1.5}\text{O}_4$ sample, 4D-STEM analysis was performed to determine the phase distribution. The technique involves recording convergent beam electron diffraction patterns in a 2D grid of electron probe positions. Data processing can be used to provide information on material properties including phase, orientation, strain, and electromagnetic field distribution.^[52] The 4D-STEM results in Figure 6b,c clearly distinguished the spinel phase and the monoclinic phase (Li_2MnO_3 -like) distribution, with the corresponding orientation map displaying polycrystallinity of the whole region and the stacking domains in the Li_2MnO_3 phase. The HAADF-STEM images (Figure 6d–g) of the same area showed contrasting regions, where atomic-resolution images revealed the typical Li_2MnO_3 -like superstructure domains along the $[110]/[100]$ direction in the dark area and spinel phase in the bright area along the $[112]$ projection, forming a coherent interface. An incoherent interface formed by the Li_2MnO_3 domains (projected $[110]/[100]$) and spinel phase (projected $[111]$) as observed in another region (Figure S7, Supporting Information). The energy dispersive spectroscopic (EDS) maps in this region exhibited the nonuniform distribution of the elements, as shown in Figure S8, Supporting Information, with higher Mn concentrations in the dark regions and higher Fe and Ni concentrations in the bright regions. These results are consistent with the 4D-STEM observations.

2.4. In Situ PXRD

As a final step, the sample $\text{LiFe}_{0.5}\text{Mn}_{1.5}\text{O}_4$ and the sample $\text{LiNi}_{0.2}\text{Fe}_{0.3}\text{Mn}_{1.5}\text{O}_4$ were subjected to in situ electrochemical PXRD, as shown in Figure 7. The two samples were chosen

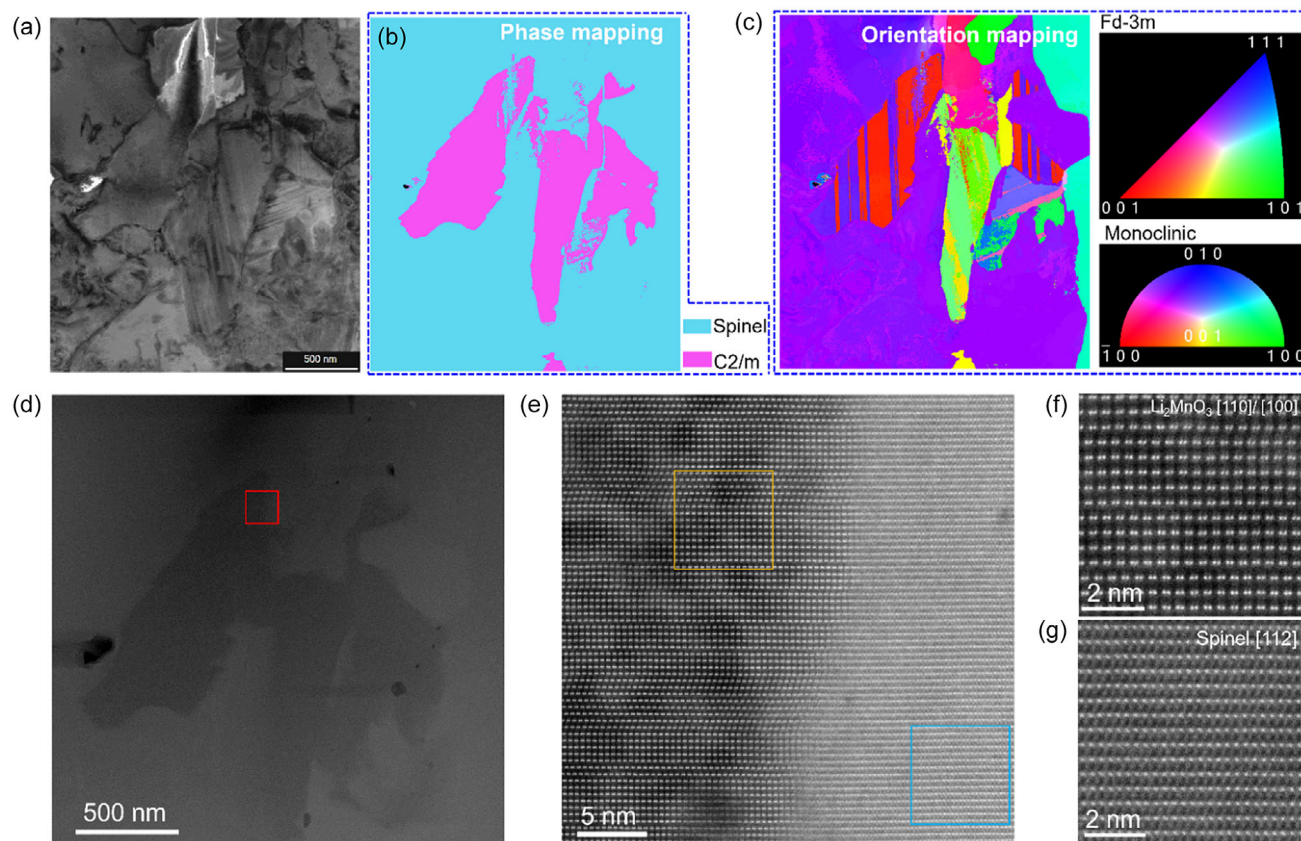


Figure 6. a) Virtual BF image of the $\text{LiNi}_{0.2}\text{Fe}_{0.3}\text{Mn}_{1.5}\text{O}_4$ sample. b,c) Phase map and orientation map of the sample shown in (a). d) The low-magnification HAADF-STEM image of $\text{LiNi}_{0.2}\text{Fe}_{0.3}\text{Mn}_{1.5}\text{O}_4$ sample. e) High-resolution HAADF-STEM image of the marked area in (d). f,g) The magnified versions of areas in (e), showing the atomic arrangement of Li_2MnO_3 phase along the $[110]/[100]$ projection, and the spinel phase along the $[112]$ projection, which formed a coherent interface in the sample.

because of their very different electrochemical performance. Figure 7a,d shows the recorded CV curves of the cycle during in situ PXRD. The CV is set to a very low scan rate of 0.02 mV s^{-1} , which results in one sweep being completed in 24 h. At an average current density of 5 mA g^{-1} , this corresponds to a C-rate of 0.04 C. Figure 7b,e displays the evolution of the Bragg reflection position of 111, 311, 511, and 531 during cycling. Both samples follow a solid solution type behavior and there is no apparent formation of new phases or phase transformations from the qualitative assessment. The collected scans were used for further analysis via full pattern fitting to extract the evolution of lattice parameters, quantitatively. The refined lattice parameters from the pristine powders (average structure, Figure 4) were used as starting values for the fitting based on scan 0, which was collected at the beginning of the measurement. Furthermore, the Al windows and the Al cathode substrate were modeled as three different Al layers with individual sample displacements (Figure S9 and S10, Supporting Information, provide a schema for the in situ cell setup and an example scan + fit). The obtained parameters for the Al layers and the layer displacement were fixed in the subsequent refinements of the following scans and only the spinel lattice parameter and the profile terms (representing instrument-specific parameters contributing

to the shape of the Bragg peaks) were allowed to refine. The result of the obtained lattice parameters is displayed in Figure 7c,f.

The results of the lattice parameter fitting are accompanied by the obvious evolution of the spinel Bragg reflection positions, indicating the Li extraction and insertion via solid solution mechanism for both the “low voltage” region, where the $\text{Mn}^{4+/3+}$ reaction dominates and the “high voltage” region where the $\text{Ni}^{4+/3+}$ and $\text{Fe}^{4+/3+}$ reactions dominate. This means that the spinel structure is retained and a solid solution is obtained between $x=0$ and $x=1$ in $\text{Li}_{1-x}(\text{Ni,Fe,Mn})_2\text{O}_4$ without phase transitions. This partially disagrees with the observations of Yavuz et al. where a pseudosolid solution was identified for a $\text{LiNi}_{0.4}\text{Fe}_{0.2}\text{Mn}_{1.4}\text{O}_4$ spinel.^[40] However, the experiments in that study were performed at C/2 and the authors explain the pseudosolid solution by kinetic limitations at faster rates, which is not expected at slow rates as in the current study. We further observe that the contraction of the spinel lattice during charge is 2.1% for $\text{LiFe}_{0.5}\text{Mn}_{1.5}\text{O}_4$ and at a slightly higher value (2.3%) for $\text{LiNi}_{0.2}\text{Fe}_{0.3}\text{Mn}_{1.5}\text{O}_4$, which correlates with the extraction of Li-ions and the change to smaller ionic radii of transition metal ions during oxidation. The observation of a solid solution mechanism during expansion and extraction of the spinel unit cell by more than 2% without phase transformations highlights the known

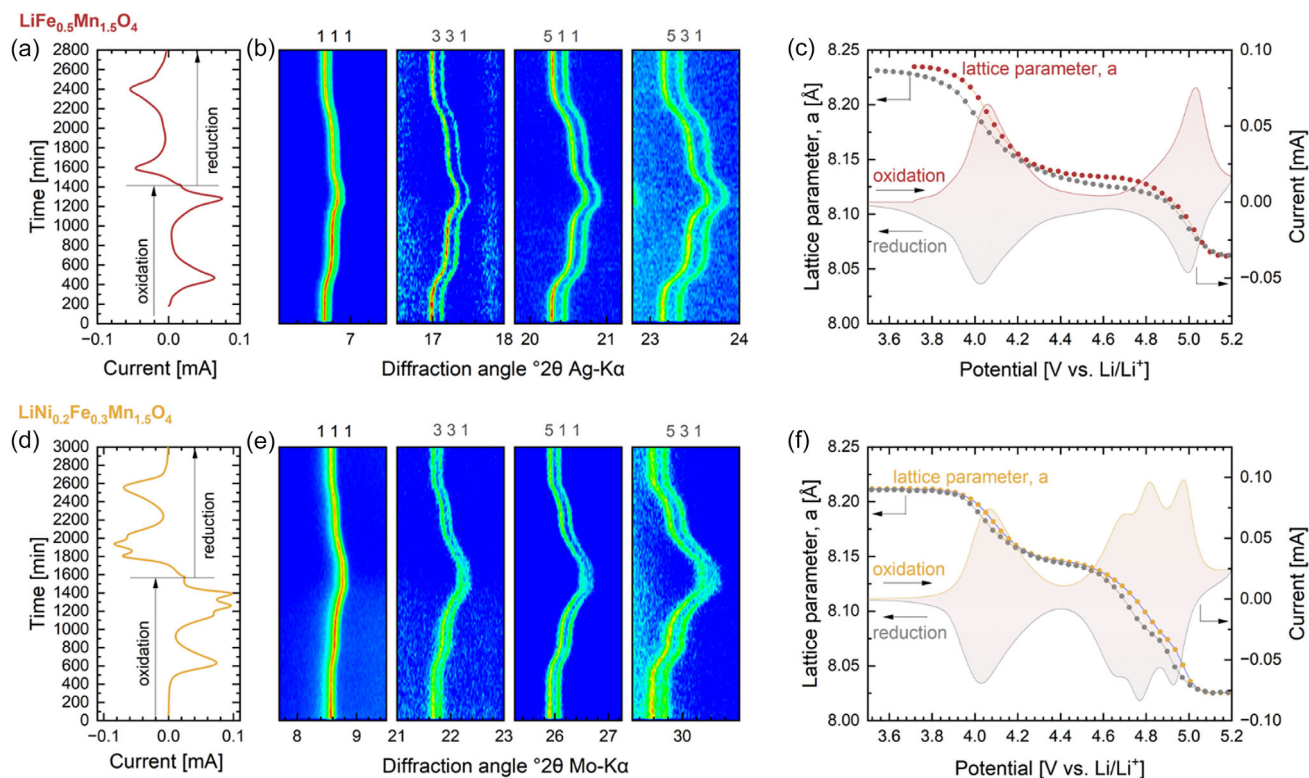


Figure 7. In situ PXRD results for $\text{LiNi}_x\text{Fe}_{0.5-x}\text{Mn}_{1.5}\text{O}_4$ ($x = 0$ and d–f) $x = 0.2$, with a,d) recorded CV at a 0.02 mV s^{-1} scanning rate during the in situ PXRD measurement. b,e) Evolution of the 111, 311, 511, and 531 reflections during oxidation and reduction. c,f) Evolution of lattice parameters during oxidation and reduction.

structural stability of Li–Mn-based spinels over a wide range of Li stoichiometry.

While the electrochemical reaction mechanism seems to be the same for both cells, there is an obvious difference between the two samples: the hysteresis of the lattice parameters within a full cycle. While for $\text{LiFe}_{0.5}\text{Mn}_{1.5}\text{O}_4$ the initial lattice parameter (8.2358 \AA) is not restored after the end of the second cycle (8.2314 \AA), it is almost completely restored for $\text{LiNi}_{0.2}\text{Fe}_{0.3}\text{Mn}_{1.5}\text{O}_4$ (8.2122 – 8.2106 \AA). This is a change of 0.054% for the lattice parameter of $\text{LiFe}_{0.5}\text{Mn}_{1.5}\text{O}_4$ after one cycle, but only 0.020% for $\text{LiNi}_{0.2}\text{Fe}_{0.3}\text{Mn}_{1.5}\text{O}_4$. Since Li-ions are extracted during charging and reinserted during discharging, while transition metals change their valence states and thus ionic radii, the change in lattice parameters reflects the change in Li-ion stoichiometry. Simply assuming a direct linear correlation between lattice parameters and the Li-stoichiometry would translate to a loss of 2.14% of Li-inventory in the $\text{LiFe}_{0.5}\text{Mn}_{1.5}\text{O}_4$ spinel electrode just within one cycle.

Recalling the electrochemical performances of $\text{LiFe}_{0.5}\text{Mn}_{1.5}\text{O}_4$ in Figure 3, we note a recorded capacity degradation of 2.34% for the full cell from cycle 1 to cycle 2. This value is in very good agreement with the calculated loss of Li inventory. With the Li-metal anode as an infinite Li reservoir, the loss of Li inventory in the cathode is the dominant degradation mechanism in the system, and the observed cell polarization can easily be interpreted as a concentration polarization in the cathode itself. The almost linear trend of the capacity decreases until the

15th cycle demonstrating that Li-ions experience the same resistance to be extracted/inserted during charge/discharge in each cycle. This continues until the capacity above 5 V versus Li/Li^+ is no longer accessible and the cycling performance stabilizes at 4 V versus Li/Li^+ . It also indicates that the concentration polarization (i.e., limit of mass transportation) is bound to the high-voltage reaction above 5 V versus Li/Li^+ .

For $\text{LiNi}_{0.2}\text{Fe}_{0.3}\text{Mn}_{1.5}\text{O}_4$, the cell polarization builds up more slowly (by one order of magnitude), leading to enhanced cycling performances as demonstrated in Figure 3b. At the same time, only 0.020% change in lattice parameter was observed within 1 cycle, which may translate to a loss of 0.78% Li in one cycle, while we recorded 0.37% loss of discharge capacity from cycle 1 to cycle 2. Obviously, these numbers are not consistent with the observed stable cycling performance of 80% capacity retention over 60 cycles. In other words, if 0.78% Li is lost per cycle, the cell would be at 80% capacity retention after 25 cycles. Thus, assuming the same degradation mechanism as for $\text{LiFe}_{0.5}\text{Mn}_{1.5}\text{O}_4$ may not be completely correct. For $\text{LiFe}_{0.5}\text{Mn}_{1.5}\text{O}_4$, we discussed that the buildup of concentration polarizations is based on the access of the $\text{Fe}^{4+/3+}$ capacity, which for $\text{LiFe}_{0.5}\text{Mn}_{1.5}\text{O}_4$ lies above 5 V versus Li/Li^+ for charging. Once the charge curves drop below 5 V versus Li/Li^+ the concentration polarization vanishes. A significant difference between $\text{LiFe}_{0.5}\text{Mn}_{1.5}\text{O}_4$ and $\text{LiNi}_{0.2}\text{Fe}_{0.3}\text{Mn}_{1.5}\text{O}_4$ is that the $\text{Fe}^{4+/3+}$ capacity can be assessed below 5 V versus Li/Li^+ during charging, almost from the first cycle. The CV scan in Figure 2c already demonstrated how

the $\text{Fe}^{4+/3+}$ for $\text{LiNi}_{0.2}\text{Fe}_{0.3}\text{Mn}_{1.5}\text{O}_4$ peak reaction was shifted below 5 V versus Li/Li^+ thus making almost the entire capacity of the electrode accessible below 5.0 V versus Li/Li^+ .

2.5. In Situ DRIFTS Analysis

In situ diffuse reflectance infrared Fourier transform spectroscopy (DRIFTS) spectrum at open-circuit voltage (OCV) over the analyte electrode was recorded to reveal the contribution of the LP30 electrolyte over electrode, as depicted in Figure S11, Supporting Information, with assignments shown in Table S3, Supporting Information. Subsequently, in situ DRIFTS spectra were recorded along the stepwise LSV and difference spectra along the potential changes were analyzed, with a schematic interpretation given in Figure 8a,b. The Ni-stabilized electrodes, namely $\text{LiNi}_{0.1}\text{Fe}_{0.4}\text{Mn}_{1.5}\text{O}_4$ and $\text{LiNi}_{0.3}\text{Fe}_{0.2}\text{Mn}_{1.5}\text{O}_4$, showed different spectral features, both in the OCV spectrum and in the difference spectra along the LSV, compared to the Ni-free $\text{LiFe}_{0.5}\text{Mn}_{1.5}\text{O}_4$ electrode. This indicates that Ni-incorporation leads to an altered surface chemistry.

In Figure 8c–e, all three cathodes had a relatively weak and clean difference spectrum in the potential range from OCV to 3.4 V versus Li/Li^+ , while new and stronger absorbance bands appeared after 3.4 V versus Li/Li^+ . This phenomenon suggests an onset of CEI formation initiated by a potential scan in the range of 3.4–3.8 V versus Li/Li^+ , which is close to the onset of the $\text{Mn}^{3+}/\text{Mn}^{4+}$ transition. Though the onset potential of CEI was similar, the difference spectra revealing CEI formation

after 3.4 V versus Li/Li^+ were obviously different when Ni was incorporated into the cathode spinel structure. The CEI species based on band assignments will be discussed below. Figure 8c–e shows that the difference spectra showing CEI formation were similar along the LSV over each electrode, and the similar difference spectra continued in the second delithiation cycle as shown in Figure S12, Supporting Information. This indicates an accumulation of similar surface species along the LSV after CEI formation was initiated.

In Figure 8c, the difference spectra over $\text{LiFe}_{0.5}\text{Mn}_{1.5}\text{O}_4$ in the 3.4 V-OCV range showed weak bands at 1773 ($\nu \text{C=O}$) and 1293 ($\nu \text{C-O-C}$) cm^{-1} from polarized EC and DMC. The difference spectra in the 3.8–3.4 V versus Li/Li^+ range revealed absorbance bands from species from the oxidative decomposition of EC. The notable surface species includes vinylene carbonate (VC), acyl fluoride (ROCOF), PF_x^- , Li-alkyl carbonates (ROCO_2Li), Li-ethylene dicarbonate ($(\text{CH}_2\text{OCO}_2\text{Li})_2$), CH_3OLi , and LiCO_3 . The bands observed at 1970/1866 ($\nu \text{C=O}$), 1557 ($\nu \text{C=C}$), and 1038 cm^{-1} ($\nu \text{C-O}$) can be attributed to VC, which could be formed by the proton abstraction from EC, leading to a C=C bond in its ring structure. This assignment is consistent with previous reports.^[53,54] Additionally, the bands at 1828 ($\nu \text{C=O}$), 1335 ($\nu \text{C-F}$) and 1230 ($\nu \text{C-O}$) cm^{-1} can be assigned to acyl fluoride from EC oxidative decomposition involving PF_6^- as previously reported by Teshager et al.^[55] The band at 869 cm^{-1} ($\nu \text{P-F}$) is attributed to the associated PF_x^- species formed from PF_6^- .^[55,56] The formation of Li-alkyl carbonates (ROCO_2Li) typically observed from EC decomposition is revealed by the bands

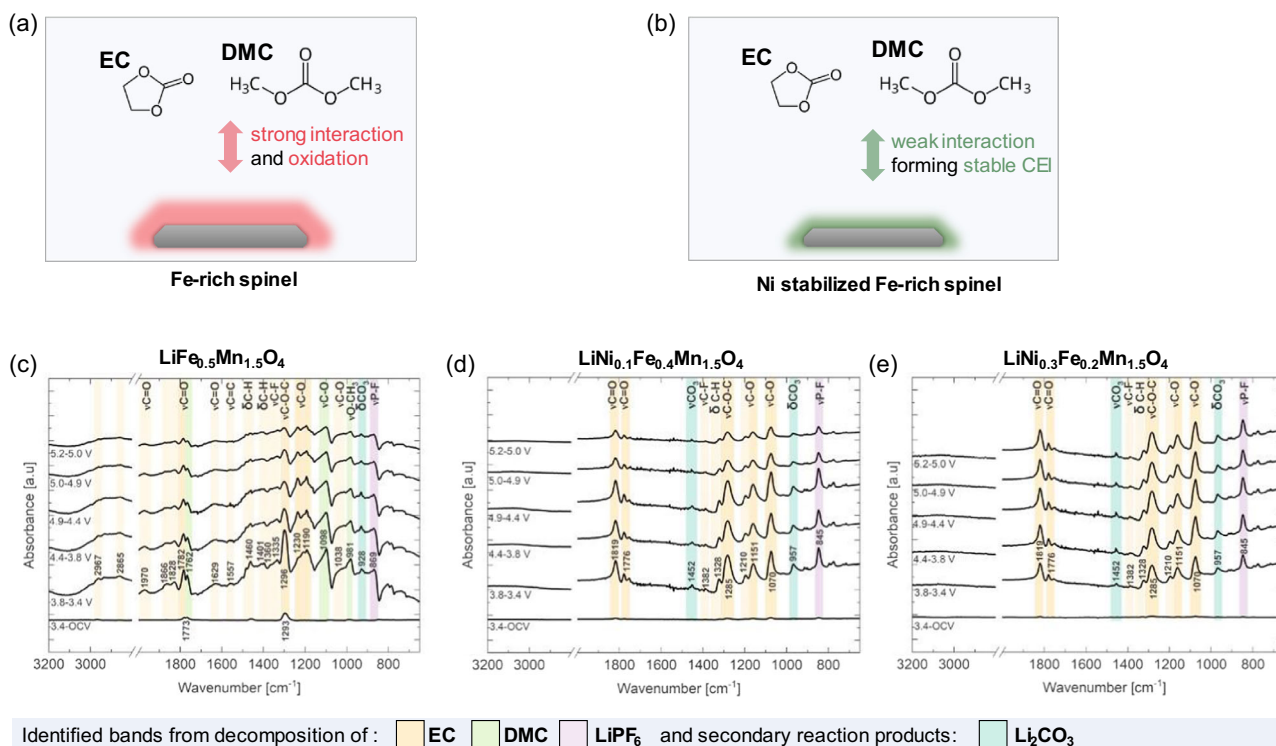


Figure 8. In situ DRIFTS difference spectra of LP30 during delithiation over a) $\text{LiFe}_{0.5}\text{Mn}_{1.5}\text{O}_4$, b) $\text{LiNi}_{0.1}\text{Fe}_{0.4}\text{Mn}_{1.5}\text{O}_4$, and c) $\text{LiNi}_{0.3}\text{Fe}_{0.2}\text{Mn}_{1.5}\text{O}_4$. Schematics for the interaction between LP30 electrolyte and CEI formation for d) Fe-rich $\text{LiFe}_{0.5}\text{Mn}_{1.5}\text{O}_4$ spinel and e) Ni-stabilized $\text{LiNi}_x\text{Fe}_{0.5-x}\text{Mn}_{1.5}\text{O}_4$ spinel.

at 2967 (ν C—H), 1782 (ν C=O), 1460 (δ C—H), 1296 (ν C—O—C), and 1098 (ν C—O) cm^{-1} similar to previous reports.^[55,56] In addition, the presence of Li-ethylene dicarbonate ((CH₂OCO₂Li)₂), a product of EC decomposition, was indicated by the bands at 2865 (ν C—H), 1629 (ν C=O), 1401 (δ C—H), 1360 (ν as C—O), 1296 (ν C—O—C), and 1190 (ν s C—O) cm^{-1} .^[57,58] The Li₂CO₃ formation was indicated by bands at 1452 (ν CO₃, overlap with δ C—H) and 928 (δ CO₃) cm^{-1} . The bands at 1762 (ν C=O), 1098 (ν C—O), and 981 (ν O—CH₃) were attributed to CH₃OCO₂Li/CH₃OLi consistent with the decomposition species of DMC.^[59] These CEI species including VC, ROCOF, PF₆[−], ROCO₂Li, ((CH₂OCO₂Li)₂), Li₂CO₃, and CH₃OLi are consistent with the previous studies.^[55,60,61] The formation of similar species was observed in subsequent scans, indicating accumulation of CEI due to oxidative decomposition of electrolyte components with formation of oxygen intermediates.^[55,62]

Figure 8d,e shows that both Ni-containing electrodes had almost the same difference spectra along the LSV, but they were slightly different from those in Figure 8c. No significant band was observed in the 3.4 V-OCV difference spectra, indicating a weak interaction with EC and DMC. The difference spectra in 3.8–3.4 V range indicate the presence of EC decomposition products, including acyl fluoride (ROCOF), Li-alkyl carbonates (ROCO₂Li), and Li₂CO₃. The bands observed at 1819 (ν C=O), 1328 (ν C—F), and 1210 (ν C—O) cm^{-1} are attributed to the formation of ROCOF. The band at 845 cm^{-1} (ν P—F) is attributed to the stretching vibration of PF₆[−] species from PF₆.^[55,58] The bands observed at 1776 (ν C=O), 1382 (δ C—H, weak band), 1285 (ν C—O—C), and 1070 (ν C—O) cm^{-1} show the formation of ROCO₂Li with simultaneous appearance of bands related to the accompanying byproduct Li₂CO₃ at 1452 (ν CO₃) and 957 (δ CO₃) cm^{-1} .^[56,57] The subsequent scan to a higher potential showed similar spectra with weaker signals. However, similar difference spectra prevailed in the 2nd delithiation cycle, indicating the continuous formation of CEI species. There was no evidence of VC formation over the two Ni-stabilized cathodes while VC was observed over LiFe_{0.5}Mn_{1.5}O₄. The decomposition product of DMC was also not observed over the two Ni-stabilized electrodes. In addition, the ν C—H band was not observed and the δ C—H band was weak over the two Ni-containing cathodes. This implies a relatively low concentration of those CEI species containing alkyl groups, e.g., ROCOF and ROCO₂Li, compared to that observed over LiFe_{0.5}Mn_{1.5}O₄. The results suggest that Ni-inclusion in the LiFe_{0.5}Mn_{1.5}O₄ spinel leads to a decreased surface reactivity toward the oxidative decomposition of electrolyte components.

3. Conclusion

In this study, Ni substitution for Fe is used to stabilize Fe-rich high-voltage spinels and to explore the electrochemical degradation mechanism of LiFe_{0.5}Mn_{1.5}O₄ from an electrochemical and structural point of view. While LiFe_{0.5}Mn_{1.5}O₄ and Ni-stabilized LiNi_xFe_{0.5−x}Mn_{1.5}O₄ demonstrate comparable average structural and local structural features, it does show very significant differences in terms of cycling stability. We have found that even a moderate substitution of Ni for Fe leads to a tremendous improvement in cycle stability. While LiFe_{0.5}Mn_{1.5}O₄ fades to

50% of its initial capacity after 15 cycles, LiNi_{0.2}Fe_{0.3}Mn_{1.5}O₄ can be cycled for 60 cycles with a capacity retention of 79%. This is a surprisingly stable behavior for a high-voltage spinel that provides 54 mAh g^{−1} above the stability limit of the liquid electrolyte for full access to the Fe^{4+/3+} capacity. Here, we could show that the cycling mechanism for LiFe_{0.5}Mn_{1.5}O₄ and Ni-stabilized LiNi_{0.2}Fe_{0.3}Mn_{1.5}O₄ follows a solid-solution type mechanism from the evolution of spinel lattice parameters in situ PXRD. We further demonstrated that for LiFe_{0.5}Mn_{1.5}O₄ the buildup of large concentration polarizations leads to the loss of Li-inventory in each cycle and explains the very fast capacity degradation of LiFe_{0.5}Mn_{1.5}O₄. The large cell polarization is probably caused by a strong solvent–electrode interaction, which leads to an unfavorable and unstable CEI formation mechanism under oxidative reactions. The CEI formation can be effectively stabilized by Ni doping, thus allowing access to the Fe^{4+/3+} capacity in Ni-stabilized LiNi_xFe_{0.5−x}Mn_{1.5}O₄.

4. Experimental Section

Synthesis: LiNi_xFe_{0.5−x}Mn_{1.5}O₄ (LNFMFO) samples with $x = 0, 0.1, 0.2, 0.3, 0.4$, and 0.5 (Figure 1b) were prepared by solid-state reaction synthesis as described previously.^[29] Stoichiometric amounts of Li₂CO₃ (Sigma-Aldrich, ≥99%) including 2% Li-excess, MnO₂ (Alfa-Aesar, 99.9%), NiO (Alfa-Aesar, 99%), and Fe₂O₃ (Sigma-Aldrich, 99%) were weighted and then planetary ball milled for 2 h for homogenization, using 2-propanol, polytetrafluoroethylene (PTFE) container and zirconia balls. The 2-propanol was removed from the dispersion in a rotational evaporator after the ball milling. The powder mixtures were calcined in a muffle furnace under air in closed alumina crucibles at 800 °C with 48 h of dwell time and were free cooled to room temperature without specified control (by switching of the furnace).

Electrode Preparation and Electrochemical Analysis: For the cell preparation, positive electrode tapes were fabricated from the as-synthesized spinel powders. The spinel powders (80 wt%) were mixed with carbon Super P (Alfa-Aesar) (10 wt%) and polyvinylidene fluoride (PVDF) (Alfa-Aesar) (10 wt%), dissolved in N-methyl-2-pyrrolidone (NMP) (Alfa-Aesar), using a THINKY mixer. The obtained slurry was tape cast onto aluminum foils (GoodFellow) with a wet state film thickness of 150 μm and dried at 80 °C in air. Afterward, the cathode sheets were calendared, punched into 12 mm diameter disks, and further dried under vacuum at 100 °C. The battery cells were assembled inside a glove box (MBraun Ecolab) under argon atmosphere. Li-foil (Alfa-Aesar) served as the negative electrode, while glass microfiber (Whatman GF/D) and a polypropylene membrane (Celgard 2500) were used as the separator and 1 M LiPF₆ in (vol 1:1) ethylene carbonate and dimethyl carbonate (EC/DMC) (battery grade, Sigma-Aldrich) was utilized as the electrolyte. For the electrochemical testing, Swagelok-type cells were used. For the in situ powder X-ray diffraction (PXRD) experiments, self-designed CR2032 coin cells with laser-cut window of $\varnothing 6$ mm on each side sealed with aluminum foil by hot glue (Acrylate, STEINEL) were used.

Electrochemical testing protocols on the samples in Swagelok-type cells employed CV at a scan rate of 0.02 mV s^{−1} in a voltage range of 3.5–5.2 V versus Li/Li⁺ and galvanostatic charge–discharge at C/5 in a voltage range of 3.5 V–5.2 V versus Li/Li⁺ by using a VMP 300 potentiostat (Biologic) within a climate chamber set at 25 °C. For the in situ PXRD measurements, the prepared coin cells were conditioned and controlled via measuring the OCV for 20 h on each cell, followed by 1 cycle of CV at a scan rate of 0.02 mV s^{−1} in a voltage range of 3.5–5.2 V versus Li/Li⁺ at a potentiostat (MPG-2, Biologic) within a climate chamber set at 25 °C. The in situ PXRD was collected from the as-conditioned cell in its second cycle through CV with a potentiostat (SP-300, Biologic).

Chemical and Microstructural Analysis: The quantification of cation contents of the spinel powders was carried out by using inductively coupled

plasma optical emission spectroscopy (ICP-OES), as described previously.^[20] Each digestion was measured twice and the mean result of three emission lines per element was used for quantification. For microstructural analysis, the as-prepared powders were investigated with an SEM (Quanta FEG 650 FEI, USA). The images were recorded by operating the SEM at an accelerating voltage of 20.0 kV with a secondary electron detector.

Powder X-Ray Diffraction and In Situ X-Ray Diffraction: PXRD was carried out on the spinel powder samples at an EMPYREAN (Panalytical) diffractometer in Bragg–Brentano geometry using Cu-K α radiation ($\lambda = 1.5418 \text{ \AA}$) and a Ni-filter for K β elimination. The diffractograms were collected in a 2θ range from 10 to 120° at 40 kV, 40 mA, with a step size of 0.008° 2θ and a counting time of 60 s per step. Laboratory hard X-ray scattering data for pair distribution function (PDF) analysis were collected with a STOE STADI P diffractometer using monochromatic Ag-K α_1 radiation, $\lambda = 0.5594 \text{ \AA}$ (Ge(111) monochromator) in Debye Scherrer Geometry using four Dectris MYTHEN2 R 1 K detectors.^[63] Samples were measured in 1 mm-diameter Kapton capillaries at a full collection time of 6 h in a Q -range of 0.5–20.4 \AA^{-1} . The PDF was calculated using pdfgetx3.^[45] Rietveld analysis^[64] and PDF analysis based on the collected hard X-ray PXRD data were carried out within the Diffraction Topas 7 (Bruker) software package. The instrumental resolution (q_{damp} , q_{broad}) was determined from a LaB $_6$ standard. All in situ PXRD measurements were performed in transmission geometry at an EMPYREAN (Panalytical) diffractometer, using Mo-K α or Ag-K α radiation ($\lambda = 0.7107 \text{ \AA}$ and $\lambda = 0.5620 \text{ \AA}$, respectively). The in situ data were collected in Debye Scherrer Geometry using the above-described self-designed coin-cell with $\phi 6 \text{ mm}$ concentric opening tightly sealed with Al-foil as the window. The quantification of lattice parameters was carried out within the Diffraction Topas 7 (Bruker) software package.

HAADF and 4D-STEM Data Collection: The transmission electron microscopy (TEM) samples were prepared by focused ion beam (FEI Helios NanoLab 460F1). The atomic HAADF imaging and energy-dispersive spectroscopy (EDS) mapping were conducted on a TFS Spectra 300 (S)TEM operated at 300 kV. The microscope is equipped with an ultrahigh brightness field emission gun, a probe aberration corrector for aberration-corrected STEM and an image aberration corrector for aberration-corrected TEM. 4D-STEM experiment was conducted on Tescan Tensor microscope, which is the world's first precession-assisted 4D-STEM microscope and can realize near real-time analysis and processing of 4D-STEM data. The 4D-STEM was performed at a convergence semi-angle of 1.5 mrad, beam current of 200 pA, and probe size of 1.5 nm. The diffraction size is 80 mrad. The precession angle is 0.8°. The electron probe was raster scanned across the selection area using a step size of 4.3 nm and a diffraction pattern was recorded at each probe position with a high-performance, hybrid-pixel, direct electron diffraction camera (Dectris Quadro). The camera has 512×512 physical pixels, and 4-fold (128×128 pixels) pixel binning is utilized for orientation and phase mapping.

In Situ DRIFTS Experiment: DRIFTS measurements were performed using Nicolet 6700 FTIR spectrometer equipped with a DRIFTS sampling accessory and mercury–cadmium–telluride (MCT/A) detector cooled with liquid nitrogen. An in-house made three-electrode system DRIFTS cell was assembled inside an argon-filled glove box ($\text{H}_2\text{O} < 0.1$, $\text{O}_2 < 1 \text{ ppm}$), using $\text{LiNi}_x\text{Fe}_{0.5-x}\text{Mn}_{1.5}\text{O}_4$ cathode material as working electrode, Pt serving as the counter and Li foil as the reference electrode. Then, the DRIFTS cell was installed in the FTIR instrument, the electrode position was adjusted until maximum signal intensity was obtained.^[57] The spectrum was recorded by accumulating 250 scans with a resolution of 4 cm^{-1} . The background spectrum was collected from the working electrode before the cell was filled with electrolyte. Then OCV was recorded from the surface of the working electrode after 20-min electrolyte flow into the cell. The thin layer of electrolyte and adsorbed species covering the electrode surface are responsible for the DRIFTS spectra at OCV. After in situ DRIFTS spectra were recorded at OCV, the potential was scanned in anode direction and DRIFTS spectra were collected at selected potentials, typically before and after oxidation signal identified in CV. The flow of electrolyte was maintained throughout experiments using a circulating pump. For in situ

DRIFTS difference spectrum analysis at the selected potential range, contributions from the adsorbed species at preceded potential were removed by subtracting the preceding DRIFTS spectrum with the subtraction coefficient factor.

Supporting Information

Supporting Information is available from the Wiley Online Library or from the author.

Acknowledgements

Funding from the German Federal Ministry of Education and Research (BMBF-project DESIREE, grant no. 03SF0477A and 03SF0477B) is gratefully acknowledged. Financial support through the Alexander von Humboldt Foundation and the National Council of Science and Technology under the grant NSTC 1120000023 is gratefully acknowledged.

Open Access funding enabled and organized by Projekt DEAL.

Conflict of Interest

The authors declare no conflict of interest.

Author Contributions

Anna Windmüller: conceptualization (equal); data curation (equal); formal analysis (equal); investigation (equal); methodology (equal); validation (equal); visualization (lead); writing—original draft (lead); writing—review and editing (lead). **Tingting Yang:** formal analysis (equal); investigation (equal); methodology (equal); visualization (supporting); writing—original draft (supporting); writing—review & editing (supporting). **Kristian Schaps:** formal analysis (supporting); methodology (supporting); writing—original draft (supporting). **Anna Domgans:** formal analysis (supporting); methodology (supporting). **Frederik Zantis:** formal analysis (supporting); methodology (supporting). **Baolin Wu:** formal analysis (supporting); investigation (supporting); methodology (equal); writing—review & editing (supporting). **Leyla Hassem Adem:** formal analysis (equal); investigation (equal); methodology (equal); writing—original draft (supporting). **Bikila Nagasa Olana:** formal analysis (equal); investigation (equal); methodology (equal); writing—original draft (supporting). **Chih-Long Tsai:** investigation (supporting); visualization (supporting); writing—review and editing (equal). **Shicheng Yu:** project administration (equal); writing—review and editing (supporting). **Luc Raijmakers:** project administration (supporting); resources (supporting); writing—review and editing (supporting). **Hans Kungl:** conceptualization (equal); data curation (equal); formal analysis (equal); funding acquisition (equal); investigation (equal); methodology (equal); project administration (equal); resources (equal); supervision (lead); validation (equal); visualization (equal); writing—review and editing (equal). **Hermann Tempel:** project administration (equal); resources (equal); supervision (equal); writing—review and editing (supporting). **Rafal E. Dunin-Borkowski:** resources (equal); supervision (equal); writing—review and editing (supporting). **Shawn D. Lin:** resources (equal); supervision (equal); writing—review and editing (supporting). **Mirjam Zobel:** investigation (equal); methodology (equal); resources (supporting); validation (equal); writing—review and editing (supporting). **Bing Joe Hwang:** investigation (supporting); resources (supporting); supervision (supporting); validation (supporting); writing—review and editing (supporting). **Rüdiger-A. Eichel:** funding acquisition (lead); project administration (supporting); resources (lead); supervision (lead); writing—review and editing (supporting).

Data Availability Statement

The data that support the findings of this study are available in the supplementary material of this article.

Keywords

Fe-rich spinel, high-voltage spinels, Li-ion batteries, Ni stabilization, structural analyses

Received: December 28, 2024

Revised: February 15, 2025

Published online: March 18, 2025

- [1] Y. E. Durmus, H. Zhang, F. Baakes, G. Desmaizieres, H. Hayun, L. Yang, M. Kolek, V. Küpers, J. Janek, D. Mandler, S. Passerini, Y. Ein-Eli, *Adv. Energy Mater.* **2020**, *10*, 2000089.
- [2] S. Dühnen, J. Betz, M. Kolek, R. Schmich, M. Winter, T. Placke, *Small Methods* **2020**, *4*, 2000039.
- [3] M. M. Thackeray, *Adv. Energy Mater.* **2021**, *11*, 2001117.
- [4] A. Kraysberg, Y. Ein-Eli, *Adv. Energy Mater.* **2012**, *2*, 922.
- [5] W. Zeng, F. Xia, J. Wang, J. Yang, H. Peng, W. Shu, Q. Li, H. Wang, G. Wang, S. Mu, J. Wu, *Nat. Commun.* **2024**, *15*, 7371.
- [6] G. Liang, V. K. Peterson, K. W. See, Z. Guo, W. K. Pang, *J. Mater. Chem. A* **2020**, *8*, 15373.
- [7] Y. Huang, Y. Dong, S. Li, J. Lee, C. Wang, Z. Zhu, W. Xue, Y. Li, J. Li, *Adv. Energy Mater.* **2021**, *11*, 2000997.
- [8] W. Tian, W. Zeng, T. Wang, J. Tian, D. Yuan, J. Wang, S. Mu, *Inorg. Chem.* **2023**, *62*, 12079.
- [9] E. Hu, S.-M. Bak, Y. Liu, J. Liu, X. Yu, Y.-N. Zhou, J. Zhou, P. Khalifah, K. Ariyoshi, K.-W. Nam, X.-Q. Yang, *Adv. Energy Mater.* **2016**, *6*, 1501662.
- [10] K. E. Sickafus, J. M. Wills, N. W. Grimes, *J. Am. Ceram. Soc.* **1999**, *82*, 3279.
- [11] A. Manthiram, *Nat. Commun.* **2020**, *11*, 1550.
- [12] T. Ohzuku, K. Ariyoshi, S. Takeda, Y. Sakai, *Electrochim. Acta* **2001**, *46*, 2327.
- [13] D. Liu, W. Zhu, J. Trotter, C. Gagnon, F. Barry, A. Guerfi, A. Mauger, H. Groult, C. M. Julien, J. B. Goodenough, K. Zaghib, *RSC Adv.* **2014**, *4*, 154.
- [14] J. Molenda, J. Marzec, K. Swierczek, W. Ojczyk, M. Ziemnicki, B. Molenda, M. Drozdek, R. Dziembaj, *Solid State Ion.* **2004**, *171*, 215.
- [15] K. Amine, H. Tukamoto, H. Yasuda, Y. Fujita, *J. Power Sources* **1997**, *68*, 604.
- [16] A. Windmüller, T. Renzi, H. Kungl, S. Taranenko, E. Suard, F. Fauth, M. Duttine, C.-L. Tsai, R. Sun, Y. E. Durmus, H. Tempel, P. Jakes, C. Masquelier, R.-A. Eichel, L. Croguennec, H. Ehrenberg, *J. Electrochem. Soc.* **2022**, *169*, 70518.
- [17] A. Bhaskar, N. N. Bramnik, A. Senyshyn, H. Fuess, H. Ehrenberg, *J. Electrochem. Soc.* **2010**, *157*, A689.
- [18] M. P. Pico, I. Álvarez-Serrano, M. L. López, M. L. Veiga, *Dalton Trans.* **2014**, *43*, 14787.
- [19] A. Bhaskar, N. N. Bramnik, D. M. Trots, H. Fuess, H. Ehrenberg, *J. Power Sources* **2012**, *217*, 464.
- [20] A. Windmüller, C.-L. Tsai, S. Möller, M. Balski, Y. J. Sohn, S. Uhlenbruck, O. Guillon, *J. Power Sources* **2017**, *341*, 122.
- [21] A. Windmüller, C. A. Bridges, C.-L. Tsai, S. Lobe, C. Dellen, G. M. Veith, M. Finsterbusch, S. Uhlenbruck, O. Guillon, *ACS Appl. Energy Mater.* **2018**, *1*, 715.
- [22] B. E. Murdock, J. Cen, A. G. Squires, S. R. Kavanagh, D. O. Scanlon, L. Zhang, N. Tapia-Ruiz, *Adv. Mater.* **2024**, *36*, 2400343.
- [23] D. Callegari, M. Coduri, M. Fracchia, P. Ghigna, L. Braglia, U. Anselmi Tamburini, E. Quartarone, *J. Mater. Chem. C* **2022**, *10*, 8994.
- [24] M. Song, S. U. Ahn, S. G. Kang, S. H. Chang, *Solid State Ion.* **1998**, *111*, 237.
- [25] E.-S. Lee, A. Manthiram, *J. Mater. Chem. A* **2013**, *1*, 3118.
- [26] J. Liu, A. Manthiram, *J. Phys. Chem. C* **2009**, *113*, 15073.
- [27] N. Kiziltas-Yavuz, M. Yavuz, S. Indris, N. N. Bramnik, M. Knapp, O. Dolotko, B. Das, H. Ehrenberg, A. Bhaskar, *J. Power Sources* **2016**, *327*, 507.
- [28] R. Alcántara, M. Jaraba, P. Lavela, J. M. Lloris, C. Pérez Vicente, J. L. Tirado, *J. Electrochem. Soc.* **2005**, *152*, A13.
- [29] R. Sun, P. Jakes, S. Eurich, D. van Holt, S. Yang, M. Homberger, U. Simon, H. Kungl, R.-A. Eichel, *Appl. Magn. Reson.* **2018**, *49*, 415.
- [30] R. Sun, P. Jakes, S. Taranenko, H. Kungl, R.-A. Eichel, *Solid State Ion.* **2018**, *325*, 201.
- [31] J. Betz, L. Nowak, J.-P. Brinkmann, P. Bärman, M. Diehl, M. Winter, T. Placke, R. Schmich, *Electrochim. Acta* **2019**, *325*, 134901.
- [32] A. Windmüller, C. Dellen, S. Lobe, C.-L. Tsai, S. Möller, Y. J. Sohn, N. Wettengl, M. Finsterbusch, S. Uhlenbruck, O. Guillon, *Solid State Ion.* **2018**, *320*, 378.
- [33] J.-H. Kim, S.-T. Myung, C. S. Yoon, S. G. Kang, Y.-K. Sun, *Chem. Mater.* **2004**, *16*, 906.
- [34] A. Eftekhari, *J. Power Sources* **2004**, *132*, 240.
- [35] A. Bhaskar, W. Gruner, D. Mikhailova, H. Ehrenberg, *RSC Adv.* **2013**, *3*, 5909.
- [36] H. Xia, Y. S. Meng, L. Lu, G. Ceder, *J. Electrochem. Soc.* **2007**, *154*, A737.
- [37] S. Yang, D. O. Schmidt, A. Khetan, F. Schrader, S. Jakobi, M. Homberger, M. Noyong, A. Paulus, H. Kungl, R.-A. Eichel, H. Pitsch, U. Simon, *Materials* **2018**, *11*, 806.
- [38] Y.-C. Jin, J.-G. Duh, *RSC Adv.* **2015**, *5*, 6919.
- [39] Y.-C. Jin, C.-Y. Lin, J.-G. Duh, *Electrochim. Acta* **2012**, *69*, 45.
- [40] M. Yavuz, N. Kiziltas-Yavuz, A. Bhaskar, M. Scheuermann, S. Indris, F. Fauth, M. Knapp, H. Ehrenberg, *Z. Anorg. Allg. Chem.* **2014**, *640*, 3118.
- [41] T. Fu, D. Lu, Z. Yao, Y. Li, C. Luo, T. Yang, S. Liu, Y. Chen, Q. Guo, C. Zheng, W. Sun, *J. Mater. Chem. A* **2023**, *11*, 13889.
- [42] J. Molenda, M. Ziemnicki, K. Swierczek, J. Marzec, *Defect Diffus. Forum* **2005**, *242*, 65.
- [43] D. Zeng, J. Cabana, J. Bréger, W.-S. Yoon, C. P. Grey, *Chem. Mater.* **2007**, *19*, 6277.
- [44] J. Liu, A. Huq, Z. Moorhead-Rosenberg, A. Manthiram, K. Page, *Chem. Mater.* **2016**, *28*, 6817.
- [45] P. Juhás, T. Davis, C. L. Farrow, S. J. L. Billinge, *J. Appl. Cryst.* **2013**, *46*, 560.
- [46] I.-K. Jeong, R. H. Heffner, M. J. Graf, S. J. L. Billinge, *Phys. Rev. B* **2003**, *67*, 104301.
- [47] L. Masliuk, K. Nam, M. W. Terban, Y. Lee, P. Kube, D. Delgado, F. Girgsdies, K. Reuter, R. Schlögl, A. Trunschke, C. Scheurer, M. Zobel, T. Lunkenbein, *ACS Catal.* **2024**, *14*, 9018.
- [48] T. Egami, S. Billinge, *Mater. Today* **2003**, *6*, 57.
- [49] M. M. Thackeray, M. F. Mansuetto, D. W. Dees, D. R. Vissers, *Mat. Res. Bull.* **1996**, *31*, 133.
- [50] P. Strobel, F. Le Cras, L. Seguin, M. Anne, J. M. Tarascon, *J. Solid State Chem.* **1998**, *135*, 132.
- [51] Z. Xu, J. Wang, K. Zhang, H. Zheng, Z.-X. Dai, J. Gui, X.-Q. Yang, *ACS Appl. Mater. Interfaces* **2014**, *6*, 1219.
- [52] C. Ophus, *Microsc. Microanal.* **2019**, *25*, 563.
- [53] K. L. Dorris, J. E. Boggs, A. Danti, L. L. Altpeter, *J. Chem. Phys.* **1967**, *46*, 1191.
- [54] Y. Zhang, Y. Katayama, R. Tatara, L. Giordano, Y. Yu, D. Fraggadakis, J. G. Sun, F. Maglia, R. Jung, M. Z. Bazant, Y. Shao-Horn, *Energy Environ. Sci.* **2020**, *13*, 183.

- [55] M. A. Teshager, S. D. Lin, B.-J. Hwang, F.-M. Wang, S. Hy, A. M. Haregewoin, *ChemElectroChem* **2016**, 3, 337.
- [56] T. Eriksson, A. M. Andersson, A. G. Bishop, C. Gejke, T. Gustafsson, J. O. Thomas, *J. Electrochem. Soc.* **2001**, 149, A69.
- [57] B. N. Olana, S. D. Lin, B.-J. Hwang, *Electrochim. Acta* **2022**, 416, 140266.
- [58] A. M. Haregewoin, E. G. Leggesse, J.-C. Jiang, F.-M. Wang, B.-J. Hwang, S. D. Lin, *Electrochim. Acta* **2014**, 136, 274.
- [59] R. Marom, O. Haik, D. Aurbach, I. C. Halalay, *J. Electrochem. Soc.* **2010**, 157, A972.
- [60] F. Joho, P. Novák, *Electrochim. Acta* **2000**, 45, 3589.
- [61] S.-W. Song, G. V. Zhuang, P. N. Ross, *J. Electrochem. Soc.* **2004**, 151, A1162.
- [62] J. Yan, X. Liu, B. Li, *RSC Adv.* **2014**, 4, 63268.
- [63] S. L. J. Thomaes, N. Prinz, T. Hartmann, M. Teck, S. Correll, M. Zobel, *Rev. Sci. Instrum.* **2019**, 90, 43905.
- [64] H. M. Rietveld, *J. Appl. Cryst.* **1969**, 2, 65.